ACS OMEGA

http://pubs.acs.org/journal/acsodf
Article

Analyzing Burner Performance and Combustion Phenomenon in an Olefin Plant's Industrial Furnace: A CFD Study

Mohsen Fattahi, Saeed Ebrahimi, Masoud Rahimi, Maryam Gonbadi, Seyyed Hossein Hosseini,* and Goodarz Ahmadi

Cite This: *ACS Omega* 2024, 9, 14500−14519
Read Online
ACCESS | Metrics & More | Article Recommendations

ABSTRACT: This work presents a comprehensive study of the combustion performance of an industrial furnace in an olefin plant using computational fluid dynamics (CFD) simulations. The focus was on analyzing the heat release pattern of bottom burners to optimize the furnace efficiency in steam-cracking processes. The study developed an accurate computational fluid dynamics (CFD) model for predicting combustion behavior in a cracking furnace. The computational model was validated by comparing the simulation results with industrial data and was used to investigate the impact of burner clogging and the importance of small holes in the body of burners in the furnace. The results also provided insights into the influence of excess air, temperature distribution, fluid behavior, composition of combustion products, and thermal efficiency of the furnace. The presented results contributed to a better understanding of parameters controlling combustion performance in steam-cracking furnaces.

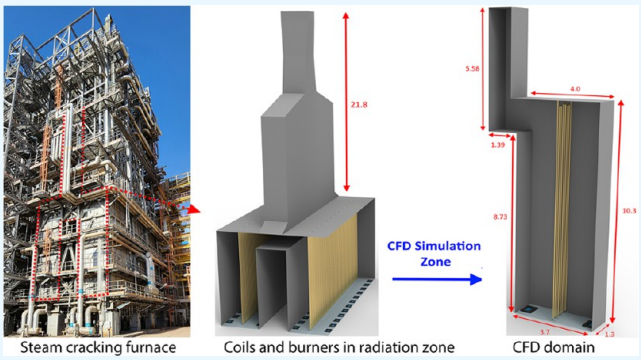

1. INTRODUCTION

Olefins are crucial components of the petrochemical industry and play a valuable role in the production of plastics and other chemical products. Among olefins, ethylene and propylene are the most important, with an annual production of roughly 1.5 × 10^8 and 8 × 10^7 t, respectively.[1] Steam-cracking furnaces are utilized to produce ethylene and propylene from light hydrocarbons combined with steam. These units consist of two main components: a coil bundle, where the cracking reactions occur, and a furnace, which is responsible for supplying heat to the coils. The cracking reactions are endothermic, requiring a significant amount of energy. Therefore, the coils are strategically positioned in the radiant section of the furnace, which maintains a temperature exceeding 800 °C and ensures sufficient supply of heat.[2] Burners at the furnace bottom or side wall provide the heat needed for the highly endothermic pyrolysis reaction in the furnace firebox. The heat release pattern of the bottom burners and the physical location of the side wall burners are critical factors in determining the furnace efficiency.[3]

The combustion performance in the radiant zone of steam-cracking furnaces is important in ensuring efficient and effective operation of these units. Achieving optimal combustion performance is crucial for maximizing the production of the desired products while minimizing energy consumption and emissions. However, industrial combustion is a complex process influenced by many factors, including heat transfer, thermodynamics, chemical kinetics, and multiphase turbulent fluid flow. Therefore, studying industrial combustion requires knowledge of multiple disciplines.[4] Researchers have employed various techniques and methodologies to study and optimize the combustion processes in these furnaces. In particular, computational fluid dynamics (CFD) simulations have been used.

CFD allows for a detailed and quantitative analysis of the flow, heat transfer, and chemical reactions within the furnace. By simulation of the flow patterns, temperature distributions, species concentrations, and combustion reactions, researchers can gain insights into the behavior of the combustion process. In addition, CFD simulations enable researchers to study the effects of various parameters, such as fuel composition, burner design, residence time, and heat transfer mechanisms, on the combustion performance. This information can then be used to optimize the design and operation of steam-cracking furnaces, leading to an enhanced efficiency, reduced emissions,

Received: January 12, 2024
Revised: February 25, 2024
Accepted: March 4, 2024
Published: March 15, 2024

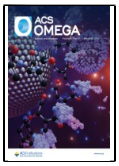

and improved product quality. Researchers often employ a combination of experimental studies and numerical simulations to enhance their understanding of the combustion process in real-world industrial settings.

Heynderickx et al.[5] and Oprins et al.[6] used three-dimensional (3D) numerical models to analyze naphtha thermal cracking furnaces. Heynderickx et al.[5] utilized a CFD model to calculate the flue gas flow pattern, temperature field in a pyrolysis furnace, and radiation models. Their findings revealed asymmetric flow patterns and uneven flue gas distributions over the furnace halves. Oprins et al.[6] performed simulations of flue gas flow fields and temperature distributions in a split coil naphtha-cracking furnace with an asymmetric flue gas outlet. They found that the compensating nature of radiative heat transfer helped maintain a nearly symmetrical temperature distribution in the furnace. Additionally, they discovered that nonuniform heating could enhance thermal efficiency and cracking results in furnaces with asymmetric flue gas outlets.

Lan et al.[7] developed a comprehensive CFD model, including the probability density function (PDF) and discrete ordinates method (DOM) for the simulation of an ethylene furnace. Simulations of an industrial ethylene furnace provided detailed information about flow and temperature fields, heat flux distribution, and species concentration distribution. Additionally, the model was utilized to examine the impacts of burner staging, tube diameter, and tube spacing on the operational performance of ethylene furnaces.

Tutar et al.[8] proposed an optimized computational fluid dynamics (CFD) modeling framework to provide an accurate representation of combustion and heat transfer in the radiation section of an industrial top-fired steam methane reforming (SMR) furnace. The proposed fully coupled 3D CFD model utilizes a detailed chemical-kinetic combustion model that accurately predicts the basic flow features.

Several models for radiative heat transfer, including the Adiabatic, P-1, Rosseland, Discrete Ordinates Model (DOM), and Discrete Transfer Radiation Model (DTRM), were investigated in the fireboxes[9] and combustion chambers.[10,11] Habibi et al.[12] studied combustion kinetics and turbulence-chemistry interaction using different radiation models. They compared the results of the Rosseland Radiation model with other radiation models and adiabatic simulations and found that the Rosseland model produced significantly different results.

Hu et al.[13] evaluated different radiation models, including the Adiabatic, P-1, discrete ordinates (DOM), and discrete transfer radiation models (DTRM). The Adiabatic model resulted in unrealistically high flue gas temperatures, and the DOM and DTRM radiation models produced similar results. Comparing the simulated results to plant design data, the DOM and DTRM performed the best, with DOM being recommended for steam-cracking furnace simulations.

Hosseini et al.[14] highlighted the importance of model selection for CFD analysis of high-temperature gas−solid reactive flow. They investigated the effects of different submodels and parameters on the accuracy of predictions and simulation time, focusing on radiation models, turbulence models, kinetic mechanisms, and other factors. The results showed that the radiation and turbulence-chemistry interaction models significantly affect temperature and composition profile predictions, especially for highly exothermic reactions. They compared the performance of different radiation models and found that the DOM and P1 models produced similar results, while the Rosseland model showed significant differences. They also reported that including radiation models increased the simulation time, with the DOM model requiring the longest time.

Industrial heating processes require significant energy, commonly generated by burning hydrocarbon fuels, such as natural gas or oil. The burners in these furnaces provide the heat required for the cracking reaction. Therefore, it is crucial to analyze the performance of burners in steam-cracking furnaces to ensure that they operate efficiently and effectively. As mentioned before, computational fluid dynamics has become an important tool in designing and operating combustion equipment such as industrial burners in steam-cracking furnaces. The main goal of using CFD in industrial burners is to reduce the cost of developing a new technology.

Wéry et al.[15] conducted a comprehensive computational investigation to optimize performance and decrease CO_2 emissions in a steam-cracking firebox-reactor coil system. The researchers paid meticulous attention to the complex geometries of the firebox and reactor coils by utilizing refined meshing techniques to accurately capture high-temperature gradients. Furthermore, they explored the effects on the heat flux distribution and tube metal temperatures. By modifying the reactor geometry, specifically by increasing the inlet slots, noteworthy enhancements in heat transfer efficiency were achieved, resulting in an impressive 82% increase in run length but with minimal changes in olefin yields. Moreover, adjustments in the flue gas excess oxygen concentration were discovered to have a crucial impact on furnace efficiency and CO_2 emission reduction, underscoring the significance of precise control and monitoring in industrial settings.

Wéry et al.[16] focused on detailed computational investigations into the influence of individual burner adjustments in the steam-cracking process. Specifically, they examined the primary-to-secondary air ratios for both floor and wall burners. Accurate simulations were conducted to capture the geometry of the firebox, including various burner configurations and coil arrangements. The simulations provided valuable insights into flame shape, temperature distribution, tube metal temperatures (TMT), run length, and emission formation under different air distribution scenarios. The results demonstrated that adjusting the primary-to-secondary air ratio significantly influenced the furnace performance. Notably, specific burner configurations showed improvements in run length and reductions in the level of NOx emissions. These findings underscore the importance of optimizing burner operation to enhance the firebox efficiency in steam-cracking processes.

This study performs a comprehensive CFD simulation of an industrial furnace in an olefin production unit, focusing on the combustion chamber zone and burners. Burner performance is crucial for furnace efficiency, and any deviations in functionality can impact the performance, energy consumption, and emissions. The study aims to understand how burner characteristics, like clogging and hole configuration, affect combustion dynamics and heat transfer. Investigating clogging effects on efficiency and hydrodynamics provides insights into optimizing burner operation. Examining burner hole configurations enhances the heat transfer efficiency. Understanding the air-to-fuel ratio for varying conditions is vital for an efficient and sustainable operation. Therefore, this study also explores the impact of different excess airflow rates on combustion behavior, providing practical endorsements for

https://doi.org/10.1021/acsomega.4c00395
ACS Omega 2024, 9, 14500−14519

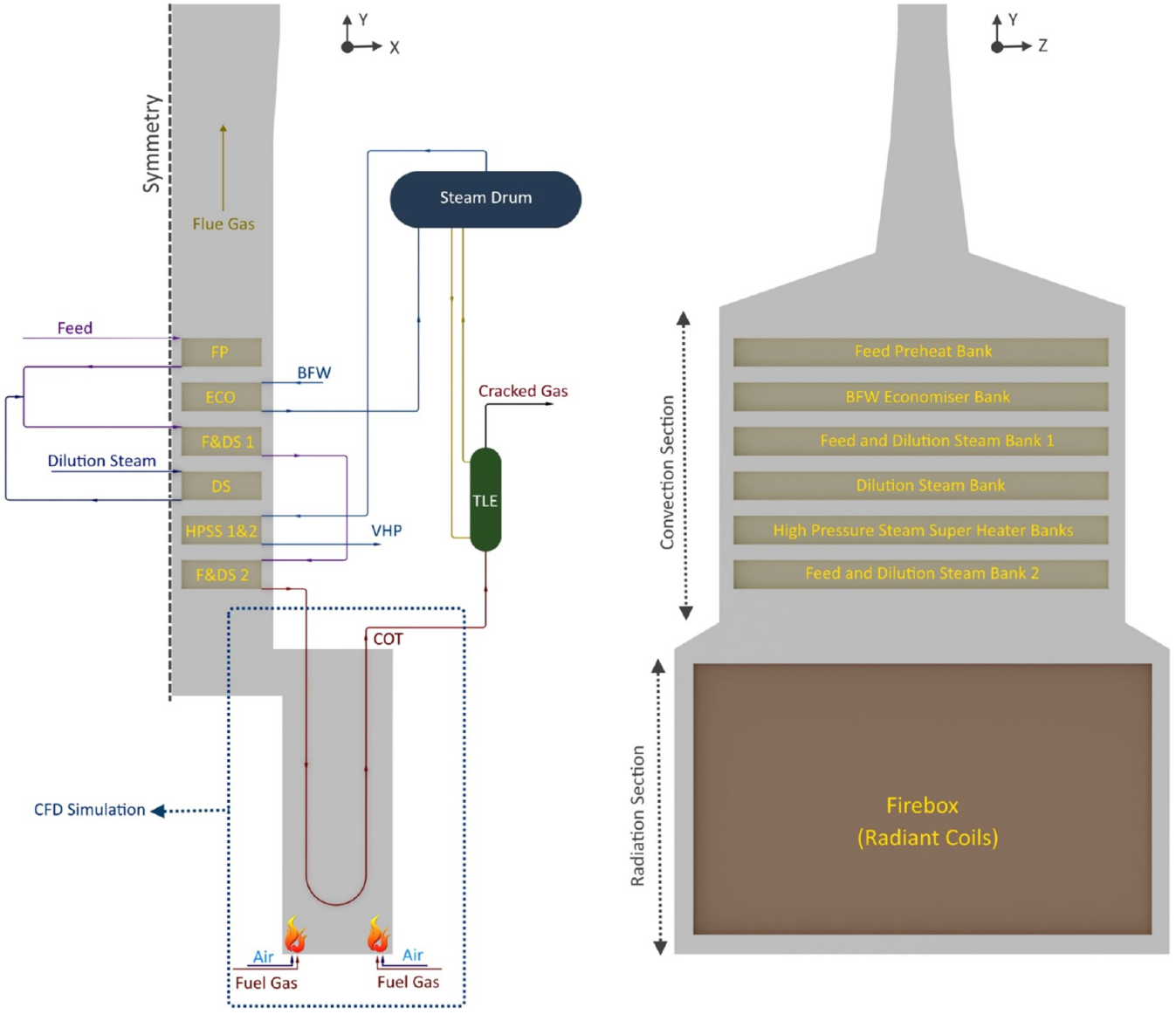

Figure 1. Schematic representation of an industrial steam-cracking furnace.

optimizing the furnace efficiency. Accurate CFD models are selected, and validation ensures reliable simulations.

2. CASE STUDY

In this investigation, an industrial furnace within an olefin unit was examined, as depicted in Figure 1. Industrial cracking furnaces have been crucial in producing raw materials for polymeric units like polyethylene and polypropylene. Figure 1 illustrates that these furnaces consist of two main sections, convection and radiation heat transfer regions. The key focus of this study is to analyze the radiation zone or the combustion chamber. The combustion chamber within the radiation zone includes insulated walls, fuel gas inlet burners, an air inlet, and cracking coils responsible for performing the cracking reaction. This cracking reaction converts ethane and propane into valuable products such as ethylene, propylene, and other byproducts. As indicated in Figure 1, the combustion zone coils are supplied with a mixture of hydrocarbon feed and dilution steam.

Understanding the impact of burners on furnace performance requires a detailed examination of their geometric complexities. However, this necessitates a more complex computational grid, leading to increased computational expenses. Additionally, since the present simulation model aims to replicate the three-dimensional nature of these systems, conducting simulations effectively requires high-capacity computing resources. To address this, the Hot Steam Standby (HSS) mode used in steam-cracking furnaces within the olefin plant has been explored. This mode helps to reduce computational time and complexity caused by cracking reactions inside the furnace coils. Furthermore, CFD simulation predictions have been validated by using industrial data available for the hot steam standby mode. HSS prepares the furnace for service and ensures efficient operation. HSS mode is employed when the steam-cracking furnace is not in regular operation or is undergoing maintenance. The furnace is prepared for startup or shutdown without needing a hydrocarbon feed using dilution steam. In this mode, only dilution steam is supplied as input to the combustion zone coils, and a hydrocarbon feed is not used. By using dilution steam and not relying on a hydrocarbon feed, the furnaces can be prepared for service efficiently while still producing indispensable very high-

https://doi.org/10.1021/acsomega.4c00395
ACS Omega 2024, 9, 14500−14519

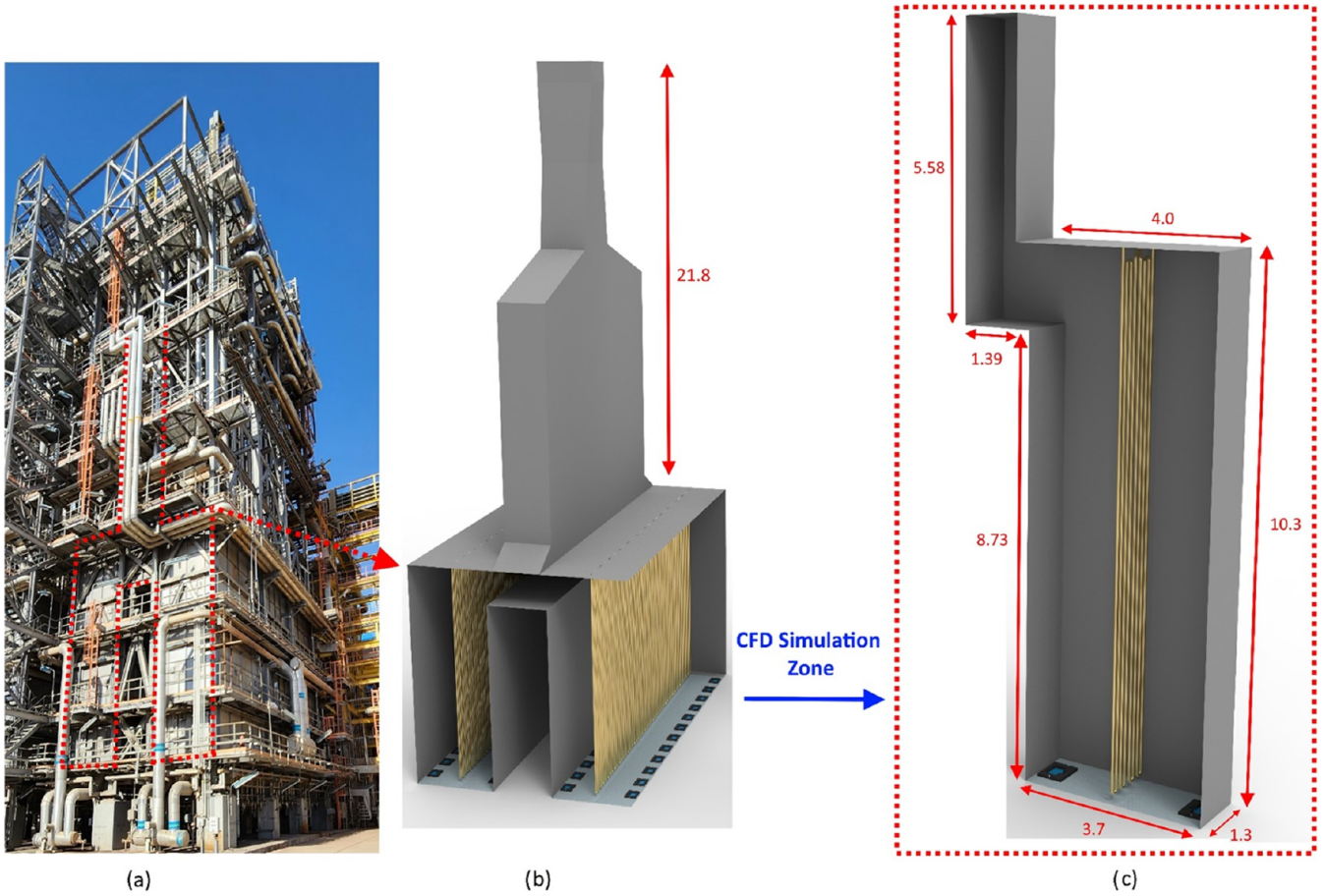

Figure 2. (a) Illustration of the industrial furnace. (b) Detailed view of coils and burner arrangements in the radiation section. (c) Selected zone for CFD investigation (units: meters).

pressure (VHP) steam in convection zones for various plant processes, including power generation, process heating, and equipment operation. The HSS mode is followed by decoke modes to remove coke from the inside of cracker tubes.

To validate the furnace simulation in HSS mode, three key parameters were examined: coil output temperature (COT), temperature of combustion gases as they exit the radiation section and enter the convection section, and flue gas temperature at the arch section.

Figure 2 shows the radiation zone, provides a layout of the cracking coils, displays details of the burners' locations, and an exterior view of the Twin Cells industrial furnace. This furnace has two separate combustion zones and a shared convection zone. Taking advantage of the furnace's geometric symmetry and strategically placed coils (as depicted in Figure 2b), a specific section of the furnace has been chosen (Figure 2c) for simulating the radiation zone. As shown in Figure 2c, the simulation zone comprises the combustion zone, a cracking coil with both inlet and outlet conduits, and a pair of fuel gas and air inlet burners. The byproduct of combustion, commonly referred to as flue gas, ascends from the combustion section's apex and enters the convection section.

The Arch temperature sensors were strategically positioned at a height of 10.9 m. However, the simulation was extended to a higher height to capture the flow development. This extension also improves the convergence. This decision was motivated by the presence of vortices and backflow in the exit area that affected flow development and posed challenges to the convergence of the numerical simulation. Simulating the flow in the enhanced computational domain with increased height leads to improved simulation convergence.

Figure 3 presents the specific dimensions and positions of the burners along with the air and fuel gas inlets. Each set consists of three burners, including the type 1 burner, which directs the flow diagonally toward the furnace wall, and the other two burners (type 2 burners), which release the fuel gas flow directly into the firebox. The inlet diameter for all burners is approximately 2 cm, with the type 1 burner featuring a nozzle head equipped with two diagonally oriented outlets, each with a diameter of around 3 mm. The outlet diameter for the type 2 burners is approximately 7.5 mm. Moreover, all burners are equipped with small holes in their bodies, each with a diameter of 1.8 mm.

3. CFD MODEL

3.1. Governing Equations. *3.1.1. Turbulent Flow.* The combustion process in industrial furnaces is a complex phenomenon that requires a detailed understanding of the flow field. The turbulent flow field within the furnace is analyzed by employing the Reynolds Averaged Navier−Stokes (RANS) model. The widely adopted renormalization group method (RNG) k-ε model[17] is used. The transport equations for mass, momentum, energy, turbulence kinetic energy, and dissipation rate are solved to evaluate the statistically stationary turbulent flow field in the furnace. The steady-state equations are

https://doi.org/10.1021/acsomega.4c00395
ACS Omega 2024, 9, 14500−14519

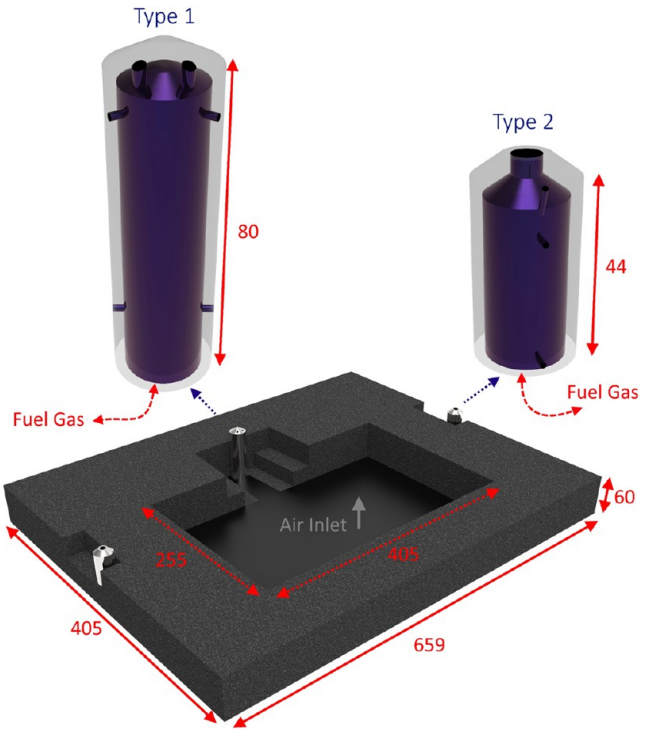

Figure 3. Detailed view of the burners in the industrial furnace investigated in this study.

$$\frac{\partial}{\partial x_i}(\rho u_i) = 0 \tag{1}$$

$$\frac{\partial}{\partial x_j}(\rho u_i u_j) = -\frac{\partial P_{\text{eff}}}{\partial x_i} + \frac{\partial}{\partial x_j}(2(\mu + \mu_t)S_{ij}) + S_{\text{Mi}} \tag{2}$$

$$\frac{\partial}{\partial x_j}(H_{\text{eff}} u_j) = \frac{\partial}{\partial x_j}\left((\lambda + \lambda_t)\frac{\partial T}{\partial x_j}\right) - \frac{\partial}{\partial x_j}\left(\sum_{m-1}^{NS} \rho(D + D_t)h_{\text{m}}\frac{\partial y_{\text{m}}}{\partial x_j}\right) + S_{\text{E}} \tag{3}$$

$$\frac{\partial}{\partial x_j}(\rho k u_j) = \frac{\partial}{\partial x_j}\left(\alpha_k(\mu + \mu_t)\frac{\partial k}{\partial x_j}\right) + P_k - \rho\varepsilon \tag{4}$$

$$\frac{\partial}{\partial x_j}(\rho\varepsilon u_j) = \frac{\partial}{\partial x_j}\left(\alpha_\varepsilon(\mu + \mu_t)\frac{\partial \varepsilon}{\partial x_j}\right) + C_{1\varepsilon}\frac{\varepsilon}{k}P_k - C_{2\varepsilon}\rho\frac{\varepsilon^2}{k} \tag{5}$$

here $P_k = 2\mu_t S_{ij}S_{ij}$; $\mu_t = C_\mu \rho k^2/\varepsilon$; $\lambda_t = \mu_t c_{\text{P}}/Pr_t$; $Pr_t = 0.9$; $C_\mu = 0.0845$; $\alpha_k = \alpha_\varepsilon = 1.39$; $C_{2\varepsilon} = 1.68$; and $C_{1\varepsilon} = 1.42 - \frac{\eta\left(1 - \frac{\eta}{\eta_0}\right)}{1 + \beta\eta^3}$; $\eta = \frac{Sk}{\varepsilon}$; $S = \sqrt{2S_{ij}S_{ij}}$; $S_{ij} = \frac{1}{2}\left(\frac{\partial u_i}{\partial x_j} + \frac{\partial u_j}{\partial x_i}\right)$

$\eta_0 = 4.38$; $\beta = 0.012$; $\rho H_{\text{eff}} = \rho E + p_{\text{eff}}$. The source term in the momentum equation includes gravitation ($S_{\text{Mx}} = S_{\text{My}} = 0$ and $S_{\text{Mz}} = -\rho g$). The source term in the energy equation is the net volumetric heat release due to radiation (Q_{rad}).

3.1.2. Radiation Model. The present study utilizes the P1 combustion model to simulate the combustion process of the industrial furnace's combustion process. This model is preferred over the DOM model due to its better convergence and less computational time. The P1 model was validated in various studies[12,18,19] Hosseini et al.[14] also confirmed that the computational time required for the DOM model is more than the P1 model time. The results of the DOM and P1 models are almost the same. The governing equations of the P1 one used in this study are as follows

$$q_{\text{r}} = -\Gamma_{\text{r}}\nabla G \tag{6}$$

$$\Gamma_{\text{r}} = \frac{1}{3(a + \sigma_{\text{s}}) - C\sigma_{\text{s}}} \tag{7}$$

$$\nabla\cdot(r\nabla G) - \alpha G + 4an^2\sigma T^4 = 0 \tag{8}$$

$$-\nabla\cdot q_{\text{r}} = aG - 4a\sigma T^4 \tag{9}$$

3.1.3. Combustion Model Equations. The turbulent combustion involves fluctuations in velocity, density, temperature, and species concentrations, making it challenging to model. For simulating turbulent combustion, various numerical approaches were developed in the past. Two widely used approaches are the PDF and the EBU models, which are computationally efficient and applicable to complex configurations.[20] However, the EBU model is only suitable for cases involving a single, perfectly premixed reactant stream.[7] In the case of the cracking furnace being studied here, air and fuel are injected separately into the firebox before combustion occurs. Therefore, the PDF model, which is widely used in the literature[7,20−23] is used in the present study to accurately model turbulent combustion. The PDF model assumes an infinitely fast and irreversible reaction, where fuel and oxidant species do not coexist in space but undergo complete one-step conversion into final products.[7] This model is suitable for simulating the combustion process in a cracking furnace. It should be mentioned that Mahmoodi et al.[24] utilized the eddy-dissipation-concept (EDC) model to simulate turbulent combustion in their CFD analysis of an industrial thermal reactor furnace within sulfur recovery units (SRUs). The EDC model exhibited good accuracy, albeit with longer computational times. In a separate study, Mahmoodi et al.[25] demonstrated that the non-premixed steady laminar flamelet model offers both time efficiency and accuracy in simulating combustion phenomena in the reaction furnace of SRUs.

The mixture fraction f is expressed as follows

$$f = \frac{m_{\text{F}} + m_0}{m_{\text{F}}} \tag{10}$$

Here, m_{F} and m_0 represent the respective mass fractions of the fuel and oxidizer, respectively.

The mixture fraction (f) transport equation describes how this quantity changes as it is transported and diffused through the flow field. The equation for the mean mixture fraction ($\overline{f}$) is given as

$$\frac{\partial}{\partial t}(\rho\overline{f}) + \nabla\cdot(\rho\overline{v}\overline{f}) = \nabla\cdot\left(\frac{\mu_t}{\sigma_t}\nabla\overline{f}\right) \tag{11}$$

In addition to the mean mixture fraction, it is essential to account for the mixture fraction variance, which describes the level of mixing in the combustion process. The transport equation for the mixture fraction variance ($\overline{f_2}$) is expressed as

https://doi.org/10.1021/acsomega.4c00395
ACS Omega 2024, 9, 14500−14519

$$\frac{\partial}{\partial t}(\rho\overline{f^2}) + \nabla\cdot(\rho\vec{v}\overline{f^2}) = \nabla\cdot\left(\frac{\mu_t}{\sigma_t}\nabla\overline{f^2}\right) + C_g\mu_t(\nabla\overline{f})^2 - C_d\rho\frac{\varepsilon}{k}\overline{f^2} \quad (12)$$

where $f' = f - \overline{f}$. The constants σ_t, C_g, and C_d are 0.7, 2.86, and 2.0, respectively.

In the non-premixed model, a probability density function (PDF) is often used to describe the statistical distribution of mixture fraction in the turbulent flow. The probability density function of the mixture fraction, denoted as $P(f)$, characterizes the likelihood of encountering a specific mixture fraction value within a specified domain. The mixture fraction (f) serves as a parameter in non-premixed combustion models, delineating the mixing ratio of fuel and oxidizer streams before ignition. The PDF is determined based on the interaction between turbulence and chemistry. It is used as a weight function to calculate average species concentrations, density, and temperature values within the flow field.

In turbulent flows, the species concentration in a reacting flow is highly fluctuating and inherently stochastic. The PDF model aims to capture these fluctuations by representing the probability distribution of these quantities. When $p(f)$ is established for each position, it serves as a weight function for determining the average values of species concentrations, density, and temperature by employing the integral equation stated below

$$\overline{\phi} = \int_0^1 \phi(f, \overline{H})p(f)\mathrm{d}f \quad (13)$$

where $\overline{H}$ is the average enthalpy.

As previously stated, the non-premixed probability density function (PDF) model utilizes mixture fraction and its variance equations to represent the behavior of individual species instead of directly solving their equations. The concentrations of the species are then determined based on the mixture fraction fields. This approach eliminates the need to solve equations for each species, which makes the model more efficient.

3.2. Boundary Conditions. Accurate simulation of the combustion process in an industrial furnace relies on accurate selection of the boundary conditions. In the present CFD simulation of the industrial furnace, the boundary conditions were carefully determined based on actual data from the industrial plant. For the fluid inlet boundary conditions, the Mass Flow Inlet boundary condition was applied to the steam (Hot Steam Standby mode), air, and fuel gas inlets of the burners. The geometric details and the values for boundary conditions were accurately calculated and provided in Tables 1 and 2, respectively. The combination of turbulence Intensity and Hydraulic Diameter has been used at the inlet boundary condition, with the hydraulic diameter calculated based on the input surface of the respective zone. Three different values of 5, 10, and 15% for the turbulence intensity were employed to investigate the effect of the inlet intensity. The results obtained for coil output and flue gas temperature from the radiation zone (Arch-T) did not exhibit significant variations; therefore, a turbulent intensity of 5% was used for the rest of the simulation. The Pressure Outlet boundary condition was used for the fluid outlet, including the coil and flue gas outlets from the radiation zone. The boundary conditions on all walls (the coil, furnace l, and burner) are the no-slip wall. The coil's

Table 1. Dimensions of the Industrial Furnace

furnace specification (radiation zone)		
	length [m] (x-direction)	3.7
	width [m] (z-direction)	1.3
	height [m] (y-direction)	10.3
	number of burners (in CFD case)	6
coil		
	coil length [m] (for 4 legs)	39.8 m
	coil diameter [mm]	63.5 (start of leg 1) - 70 (end of leg 4)
	coil outlet diameter [mm]	108
	coil wall thickness [mm]	7.5

Table 2. Operating Conditions of the Industrial Furnace

coil		value
coil inlet temperature [K]		893
coil inlet flow rate (steam) [kg/s] (for each leg)		0.13
Firing Conditions		
fuel gas flow rate [kg/s] (each zone)		0.004107
excess air [%]		0−25
fuel gas inlet temperature (K)		300
air inlet temperature (K)		300
fuel gas composition [mol %]	CH_4	77
	H_2	23
radiant zone outlet pressure [pa]		−50
Material Properties		
emissivity of the furnace wall [−]		0.75
emissivity of the coil wall [−]		0.85
thermal conductivity of coil [W/m·K]		45
thermal conductivity of bottom refractory wall [W/m·K]		0.32
thermal conductivity of top refractory wall [W/m·K]		0.16

boundary condition uses coupling to heat transfer from the radiation zone to the process fluid. Two types of wall insulation are used in the furnace: the first type up to a height of 2.5 m and the second type for the remaining height and the ceiling of the radiation zone. These variations account for the different properties of each insulation type.

The temperature of the furnace's outer walls was relatively high, indicating poor insulation. The temperature varies across different points, with an average temperature of 50 °C considered. Consequently, the heat loss generated and transferred to the environment through convection was considered in the boundary conditions for furnace wall insulation. This heat loss was calculated and incorporated into the boundary conditions. Figure 4 illustrates the selected simulation zone, which exhibits symmetry conditions on two sides in the z-direction and one side in the x-direction. The Symmetrical boundary condition was applied to these areas to ensure accurate modeling.

3.3. Computational Grid. A grid independence analysis was conducted as a preliminary step in this study to ensure the accuracy of the results. This analysis is crucial in determining the appropriate mesh size for the simulation, as using an insufficient number of meshes can lead to inaccurate results. In contrast, an excessive number of compounds can result in unnecessary computational costs.

The choice of computational cell type significantly impacts result accuracy, solution stability, and simulation time. Structured grids, composed of aligned hexahedral cells, are

https://doi.org/10.1021/acsomega.4c00395
ACS Omega 2024, 9, 14500−14519

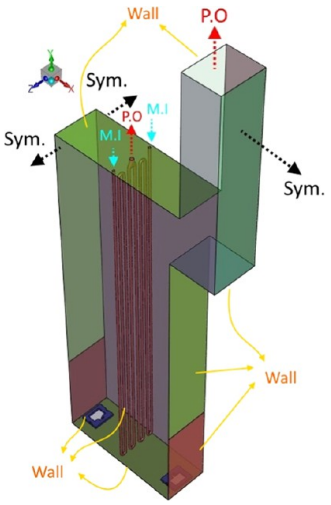

Figure 4. Boundary conditions for the computation domain.

efficient and commonly used. However, they are unsuitable for complex geometries with sharp edges and curved boundaries, as they reduce mesh quality.[14] Unstructured grids, which employ tetrahedral cells, offer an alternative. However, tetrahedral cells have limitations in excessive stretching, leading to increased element counts compared to structured grids. Polyhedral cells offer a solution by reducing cell count, improving grid quality, and enhancing calculation accuracy.[26−30] Hosseini et al.[14] extensively studied the effect of cell type on total mesh cell counts, mesh quality, simulation time, accuracy of prediction, and residuals. They found that the cell type plays a crucial role in prediction accuracy for coarse meshes, whereas the cell type effect can be ignored for fine meshes. In particular, the polyhedral mesh is preferred over other types, especially in large-scale and industrial cases with complex geometries and limited computational resources.

In the present study, first, a tetrahedral mesh was selected for the computational domain. However, the simulation was time-consuming due to the high required number of meshes and had convergence problems. Therefore, the mesh was converted from tetrahedral to polyhedral and the simulation was performed. The results showed a significant reduction in the number of meshes used, a decrease in the time required for simulation, and an improvement in the convergence process of the solution. This finding suggests that using a polyhedral mesh is advantageous for these industrial furnaces as it reduces the computational time and increases the accuracy of the simulation.

A representation of the polyhedral computational grid for the set of burners, coils, and different cross-sectional views of the firebox domain is shown in Figures 5 and 6. A polyhedral grid with varying mesh sizes was employed to capture the combustion behavior accurately in the furnace radiation zone. Specifically, finer meshes were strategically implemented in regions characterized by potentially higher gradients. These critical areas encompassed the air and fuel gas mixing zone, the fuel gas exit region from the burners, and the flue gas exit region from the firebox. Figures 5 and 6 display finer meshes in these areas, indicating an accurate method of refining the mesh to precisely represent and capture the corresponding variations in the velocity and temperature gradients.

Three meshes with different grid numbers, including fine, medium, and coarse meshes, were created, and their properties

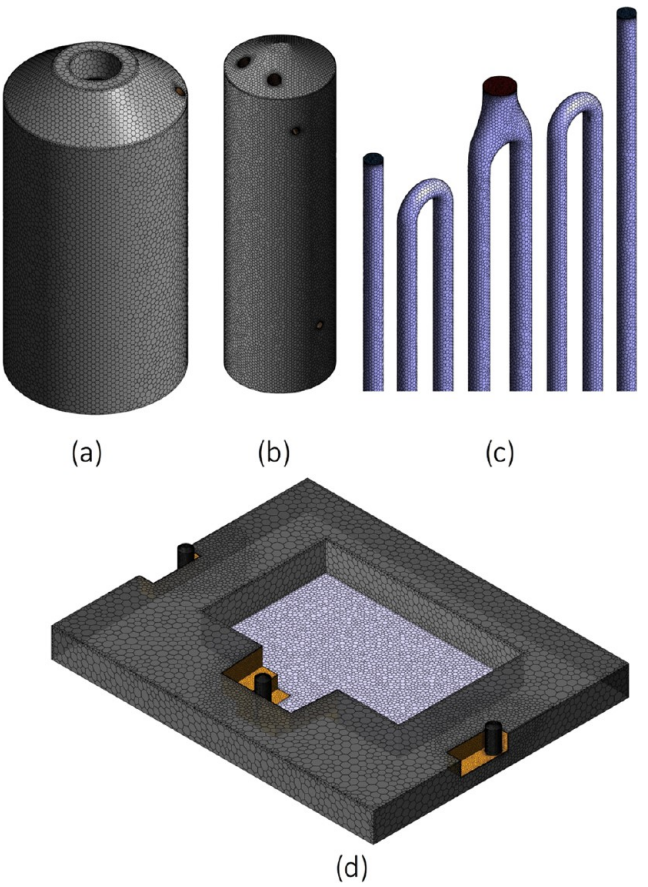

Figure 5. Polyhedral grids used in the computational domain: (a) burner (type 2), (b) burner (type 1), (c) coil, and (d) sets of burners.

are shown in Table 3. This table shows that converting the tetrahedral mesh to a polyhedral mesh reduces the number of meshes by approximately 5.5 times. However, the runtime does not decrease in the same order. This study utilized the polyhedral mesh, significantly improving the convergence process and reducing the runtime by one-third. The simulations were conducted until the errors in the energy equation were less than 10^{-6}, and the other equations were less than 10^{-3}, while the changes of the important parameters, namely, COT and the arch zone temperature, would not change with iterations and were fixed. Therefore, the number of iterations was different for each case study, with an average of at least 3000 iterations. Table 3 presents the averaged COT and arch temperature values calculated by using the polyhedral mesh.

Figure 7 illustrates the average temperature distribution of the flue gas along the furnace's height for the three different grids. This figure shows that the fine and medium meshes exhibit a similar pattern, while the coarse grid shows slightly different results. Likewise, Table 3 indicates that the coil's exit temperature and the arch zone's temperature are nearly identical for the fine and medium meshes. However, the coarse mesh, particularly in the arch area, predicts a temperature approximately 5 K higher than that of the other meshes. Additionally, despite the decreased iteration time for the coarse mesh, its convergence process was not as smooth as those of the other two meshes. It required more iterations to achieve improved convergence and stabilize the results. Ultimately, we chose the polyhedral mesh with 2,898,081

https://doi.org/10.1021/acsomega.4c00395
ACS Omega 2024, 9, 14500−14519

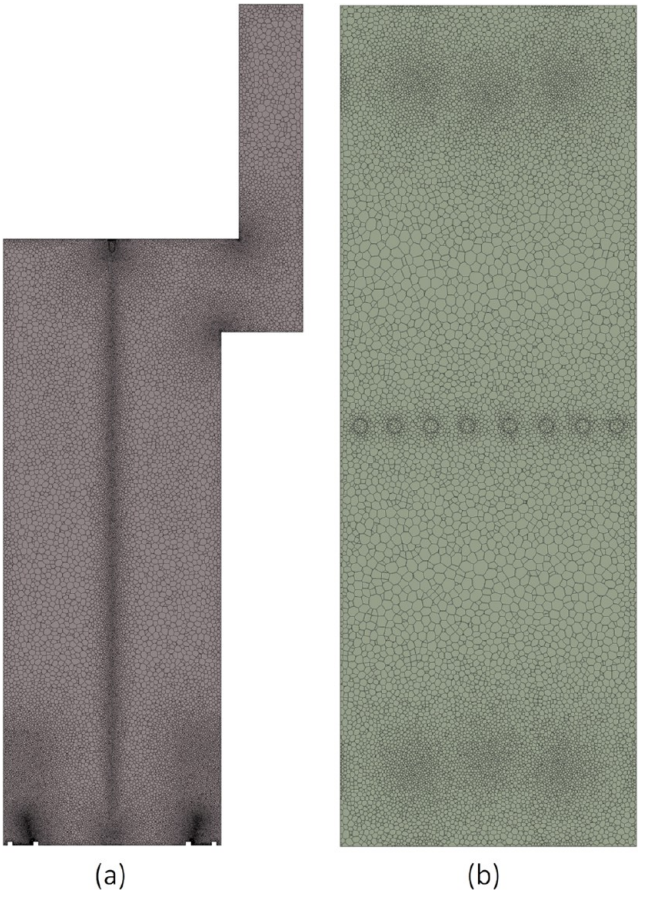

Figure 6. Polyhedral grids applied for the computational domain: (a) $X-Y$ plan and (b) $Z-X$ plan at y = 2 m.

Table 3. Coil Outlet Temperature and Arch Temperature Results for Three Different Grids to Evaluate Grid Independence (Results Are Shown Based on Polyhedral Grids)

mesh size	tetrahedral	polyhedral	COT (K)	Arch-T (K)
coarse	11,309,244	2,145,044	1071	1100.59
medium	15,933,093	2,898,081	1070.18	1095.05
fine	18,736,772	3,380,608	1070.5	1095.09

elements as the optimal choice, and the simulation continued using this mesh.

4. RESULTS AND DISCUSSION

4.1. Influence of Excess Air on CFD Simulation Results. Accurate control of the air supply is crucial for the combustion process in steam-cracking furnaces. A precise amount of excess air is required to ensure a complete combustion. In the studied furnace, negative pressure is created by using a fan at the top of the furnace stack, allowing air to enter through the air registers. Since the exact amount of oxygen in the flue gas was unknown, the simulation results were used to calculate the estimated excess air. This estimated value was considered for subsequent analyses.

Figure 8 shows the average temperature distribution of flue gas along the height of the furnace for six different values of excess air. The figure shows that the temperature distribution increases up to a height of approximately 3 m from the furnace bottom, except when there is no excess air. This indicates that most of the combustion reactions occur within this region. However, as excess air increases, the temperature gradually

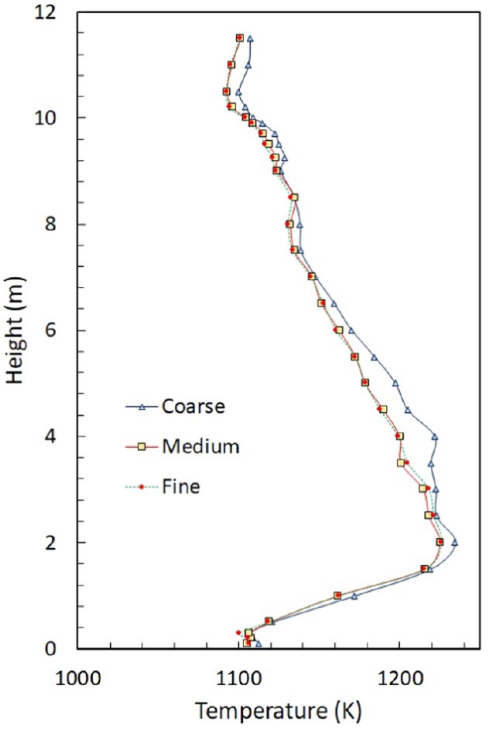

Figure 7. Results of the average temperature distribution of flue gas along the height of the furnace for three different grids.

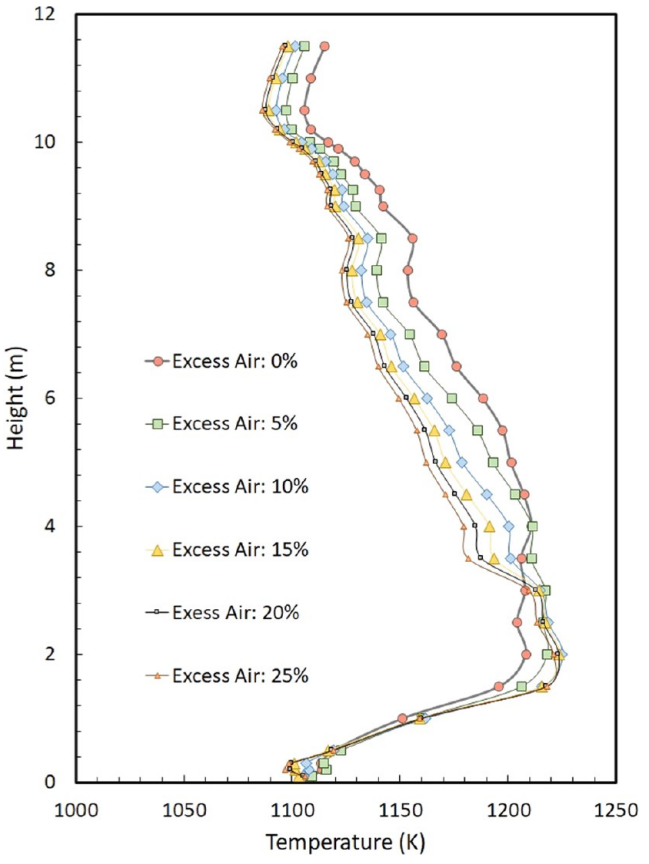

Figure 8. Average temperature distribution of flue gas along the furnace height for six different values of excess air.

https://doi.org/10.1021/acsomega.4c00395
ACS Omega 2024, 9, 14500−14519

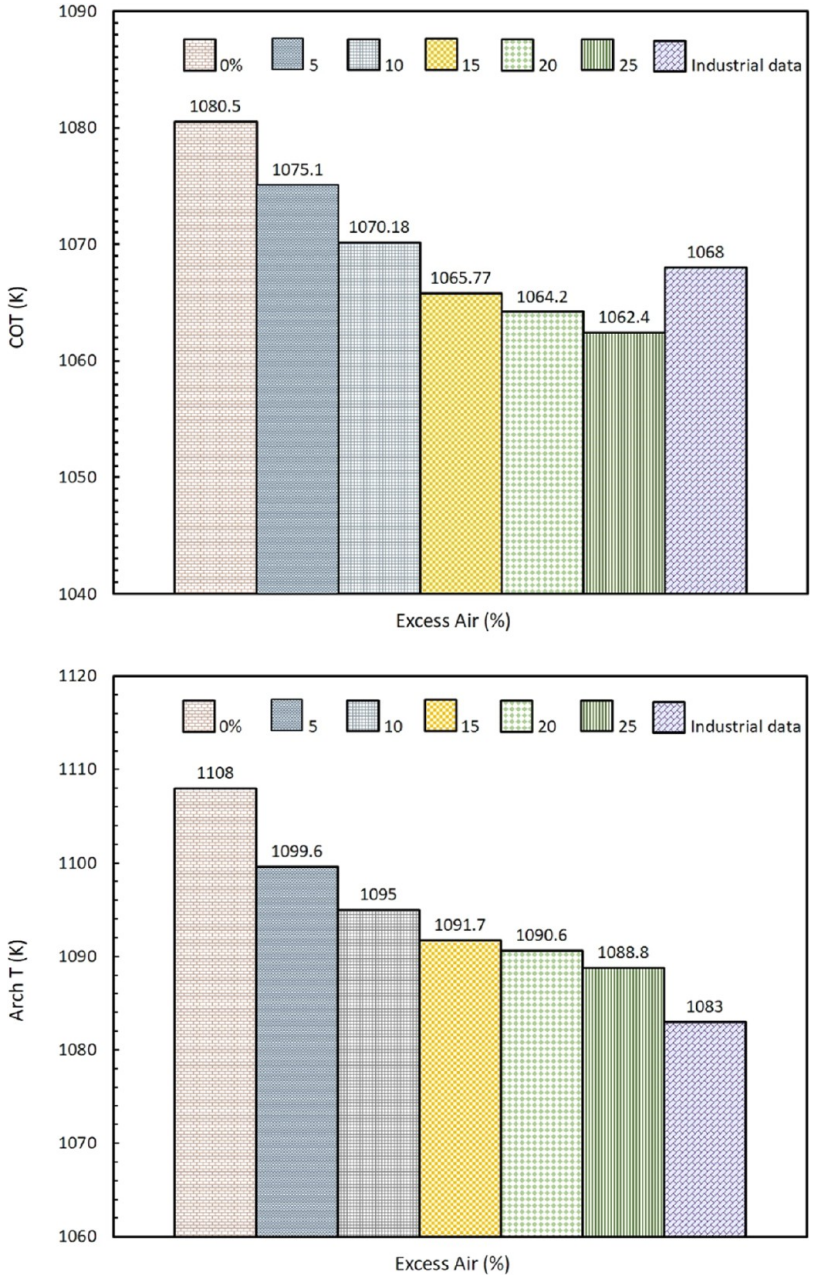

Figure 9. Simulation results of coil outlet temperature and the average temperature at the arch area for six different values of excess air compared with the measured industrial data.

decreases. This trend continues up to the top of the furnace; however, the temperature difference between different inlet excess air decreases by moving toward the top of the furnace. Therefore, the minimum temperature difference occurs at the top of the furnace, and the maximum temperature difference occurs at a height of 5 m. For each scenario, the temperature at the bottom of the furnace up to a height of 3 m increases continuously, as this zone is where air and fuel gas enter and the reaction occurs. After this area, the temperature of the flue gas decreases due to heat transfer to the fluid inside the radiant coils.

Figure 9 shows more detailed results of the COT and arch zone average temperature for different conditions. According to this figure, with the increase of excess air, the COT and the average temperature of the arch region decrease continuously. The examination reveals that CFD simulations exhibit excellent agreement with industrial data for the case of 10% excess air. To address the computational error inherent in the model, the CFD results for the coil outlet temperature and the Arch temperature are compared to industrial measurements. The analysis reveals errors of approximately 0.94 and 1.108% for these respective parameters. Based on the satisfactory agreement between the CFD findings and industrial data for the 10% excess air condition, subsequent simulations in this study were conducted using this value. It is important to note that 10% excess air is commonly employed in the industry for industrial cracking furnaces.

Figure 10 illustrates the temperature distribution contour plots of combustion compounds (flue gas) across various sections of the combustion chamber, as predicted by the CFD simulation.

https://doi.org/10.1021/acsomega.4c00395
ACS Omega 2024, 9, 14500−14519

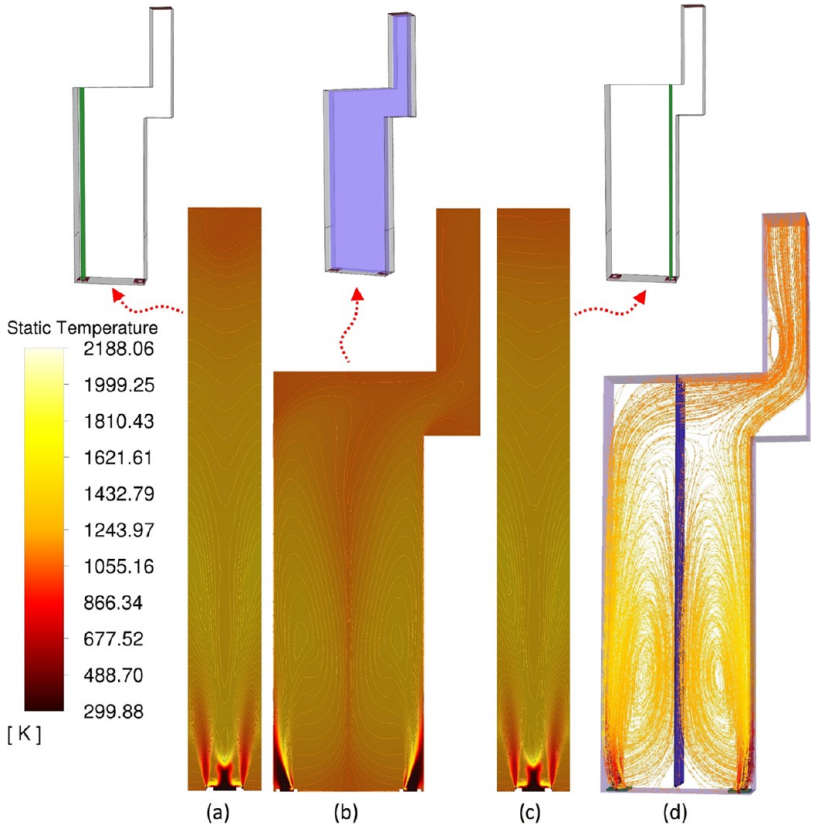

Figure 10. Contour plots of temperature distribution in the combustion zone of the furnace from three different views (a–c). (d) Streamlines of the flue gas within the furnace.

The contour plots reveal a remarkably uniform temperature distribution throughout the combustion chamber, indicating good performance of the burners. The lowest temperature is observed in the air inlet region before complete combustion. As the flue gas enters, the temperature rises, reaching a maximum value of approximately 2188 K above the burner output. Figure 10b shows that the presence of coils and the heat exchange with the flue gas lead to a localized temperature decrease in the central area of the combustion chamber at different furnace heights. Cross-sectional views in Figure 10a,c, taken in the z and y directions along the burners, exhibit nearly symmetrical behavior. Figure 10d shows that the airflow moves diagonally upon entering the furnace. This generates a tilting motion that directs the airflow toward the lateral walls. This behavior is attributed to the nozzle configuration of the type 1 burner, which features an angled trajectory of the outlet fuel gas toward the furnace walls. Consequently, the air cannot rapidly rise to the top of the furnace, promoting the initiation of the reaction. Moreover, the incorporation of holes in the body of the burners ensures the proper mixing of air with the fuel gas, facilitating a prompt reaction. This design optimally distributes and disperses the fuel gas within the combustion zone, enhancing heat transfer efficiency and promoting homogeneous mixing with the inlet air. The angled flow pattern of the burner nozzle contributes to an even and uniform distribution of heat, resulting in improved performance and enhanced productivity of the process. The strategic positioning and orientation of the burner nozzle further contribute to the creation of a well-distributed thermal environment within the furnace, enhancing process stability and overall system efficiency. Figure 10d depicts the inlet streamlines originating from the air and burner inlets, traversing the combustion zone shown in different colors due to their temperature. Symmetrical behavior is observed within the combustion chamber, contributing to temperature uniformity. However, dead zones can be formed in the upper left corner of the furnace and the flue gas exit areas, leading to a temperature decrement in those regions.

According to the streamlines, in the furnace crossover area, where flue gas exits the firebox (arch zone), vortices are formed due to a sudden change in the fluid direction, as previously mentioned. These vortices can cause backflow into the firebox, and if the output boundary condition is placed in a specific location, it can negatively affect the convergence of the solution. This backflow was prevented by extending the outlet surface area of the furnace to a higher height. This extension aims to achieve a fully developed flow, promoting a robust convergence process and effectively preventing any undesired backflow on outlet boundaries to the solution domain.

Figure 11 displays the temperature distribution contour of the coil wall, indicating that both coil passes exhibit similar and relatively symmetrical behavior. This symmetrical behavior is crucial in the combustion chamber, especially when introducing a hydrocarbon feed to the furnace, as it ensures that the cracking reaction occurs consistently within both coil passes. Additionally, Figure 11 shows that the temperature gradient changes become less observed toward the end of the coil, while the highest temperature gradient is observed at the beginning of the coil.

4.2. Burner Clogging. One of the significant challenges faced in the steam-cracking furnace industry is the issue of burner clogging. This problem arises when the burners in the

https://doi.org/10.1021/acsomega.4c00395
ACS Omega 2024, 9, 14500−14519

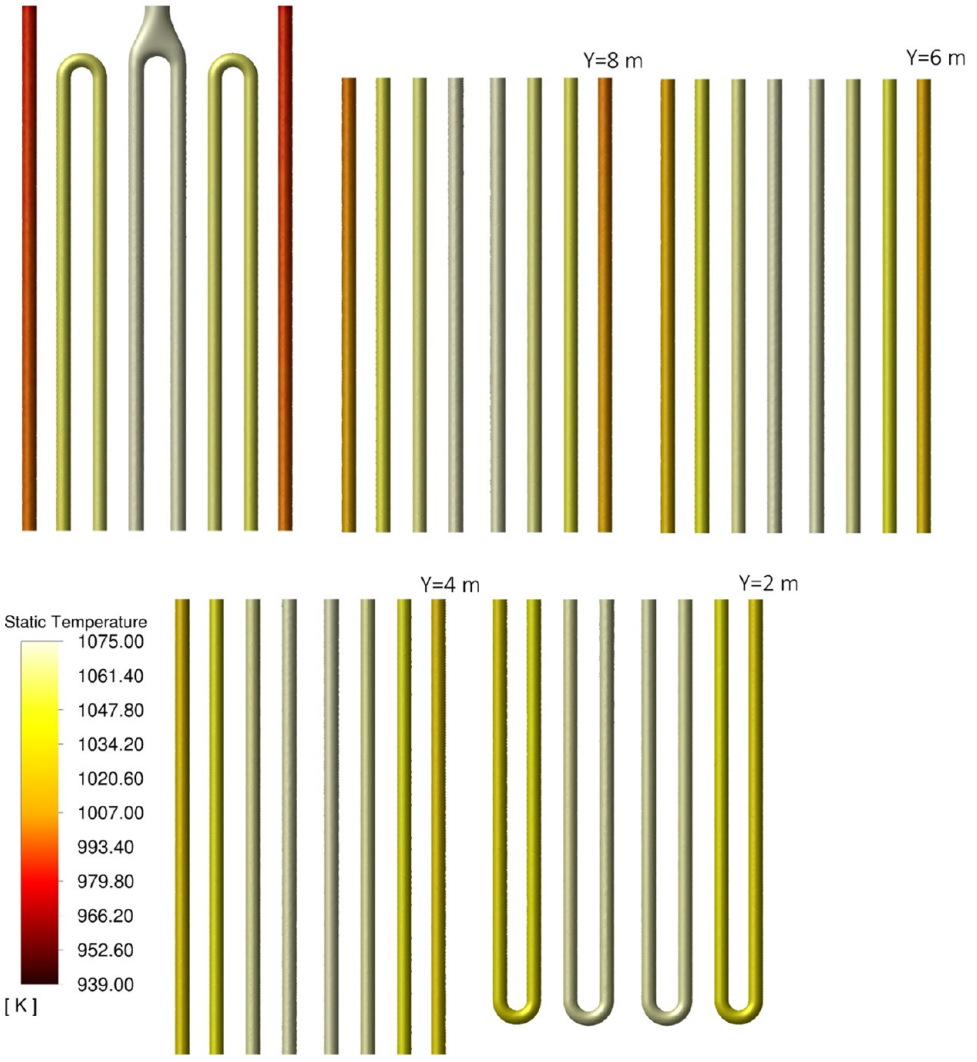

Figure 11. Contour plot of the coil wall temperature distribution.

furnace become obstructed due to various factors, such as the accumulation of carbon deposits, impurities, and contaminants in the fuel. Burner clogging can lead to a range of detrimental effects on the furnace performance and overall production efficiency. As a result, the furnace may experience flame instability, reduced efficiency, and even shutdowns.

When burners become clogged, the combustion process is disrupted, resulting in incomplete or inefficient fuel burning. This, in turn, leads to a reduced heat transfer efficiency and lower operational temperatures within the furnace. Consequently, the cracking reactions may not proceed optimally, impacting the quality and quantity of the desired end products. Moreover, burner clogging can also disrupt the uniformity of the flame distribution, causing uneven temperature profiles.

Various preventative measures can be implemented to address the burner blockage issue. It is crucial to regularly maintain and clean the burner nozzles and fuel lines to prevent carbon deposits and ensure smooth fuel flow. The use of a high-quality, purified fuel in combination with effective filtration systems can help minimize the presence of impurities and contaminants that contribute to blockage. Furthermore, implementing advanced monitoring and control systems allows for the real-time detection of potential blockage issues, enabling prompt corrective actions. In the case of cracking furnaces studied in this research, the burners are prone to blockage, necessitating continuous performance checks, periodic cleaning, and timely replacement if problems arise. The investigation revealed that severe coke deposition inside the burners is the primary cause of clogging, as depicted in Figure 12. Both type 1 and type 2 burners are susceptible to blockage, but type 1, which has an angled output and smaller output holes in the nozzle, has a higher likelihood and is more prone to blockage.

Figure 11 depicts various burners, all of which are type 1 burners. The left burner is clean, while the others are clogged. The figure reveals that severe coke formation can potentially lead to the loss of a burner nozzle cap. Thus, it becomes crucial to examine burner clogging and its impact on furnace performance, particularly during the cracking reaction. This section explores the influence of clogging on different burners, thoroughly investigating their effects on the thermal and hydrodynamic performance. For this purpose, various scenarios of burner clogging have been considered, analyzing their impact on the heat transfer distribution, hydrodynamics, and combustion product composition. The performance of these burners on the heat transfer distribution, composition of combustion products, and hydrodynamics has been shown. In

https://doi.org/10.1021/acsomega.4c00395
ACS Omega 2024, 9, 14500−14519

Figure 12. Examples of clogged burners due to severe coke formation.

the CFD simulation, it is assumed that a clogged burner results in a complete obstruction, leading to no flow.

Figure 13 displays the average temperature distribution of the flue gas along the height of the furnace for different states of burner clogging. To improve the clarity of the text regarding the arrangement of burners and different scenarios of burner clogging, they are named with English letters, and each study case is shown with the name of the blocked burner, as shown at the top of Figure 13.

In this figure, the burners exhibit similar trends when clogged, with temperatures progressively decreasing as more burners become blocked. The reduction in the inlet fuel gas flow rate, coupled with a fixed air inlet, leads to significant temperature drops, in line with industrial data showing quick temperature decreases. Burners a and b, known for their susceptibility to blockage, show a similar temperature pattern up to approximately 10 m. However, beyond that point, their temperatures diverge in the arch zone and subsequent areas. Under normal conditions (without clogging), the furnace temperature reaches its maximum of around 2 m and then decreases through heat exchange with the heating coil, transferring its energy. This behavior remains true when burners a, b, or both are clogged, considerably reducing the temperature. However, in cases with more than two clogged

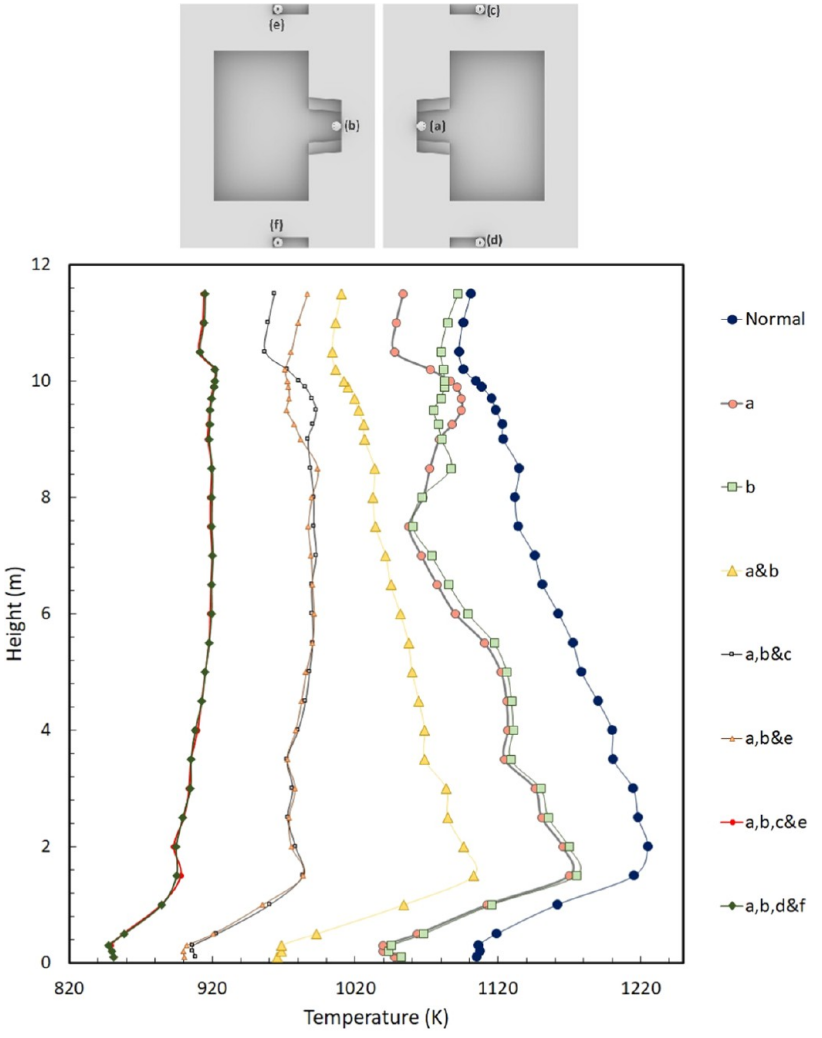

Figure 13. Average temperature distribution of flue gas along the height of the furnace for different states of burner clogging.

https://doi.org/10.1021/acsomega.4c00395
ACS Omega 2024, 9, 14500−14519

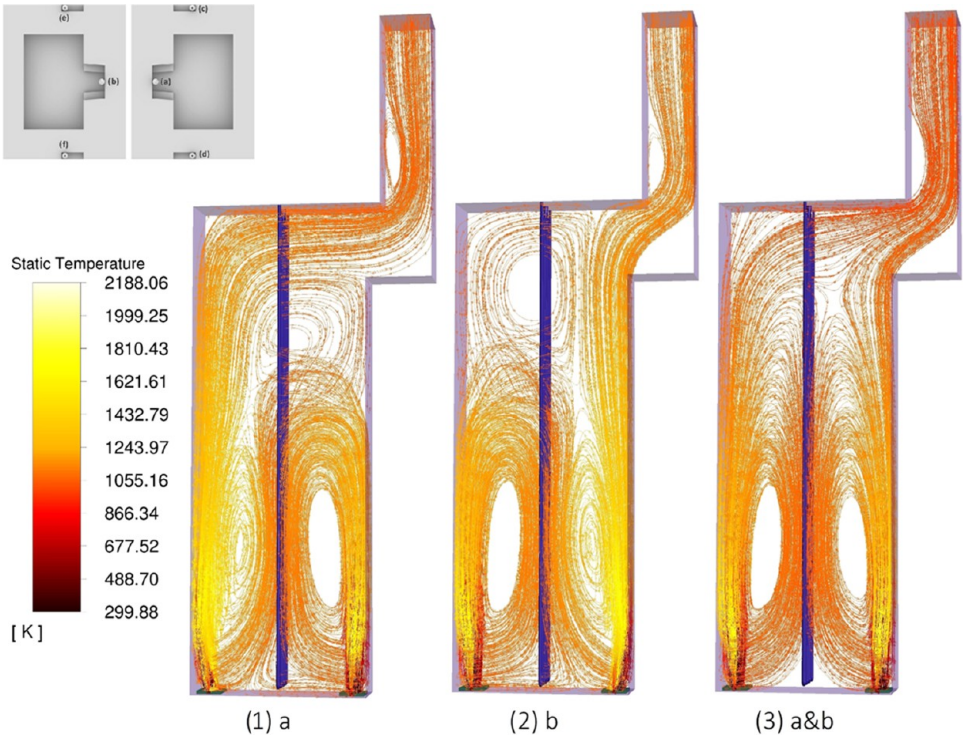

Figure 14. Streamlines of the flue gas colored by temperature within the furnace show three different states of clogging: (1) burner a, (2) burner b, and (3) burners a and b simultaneously.

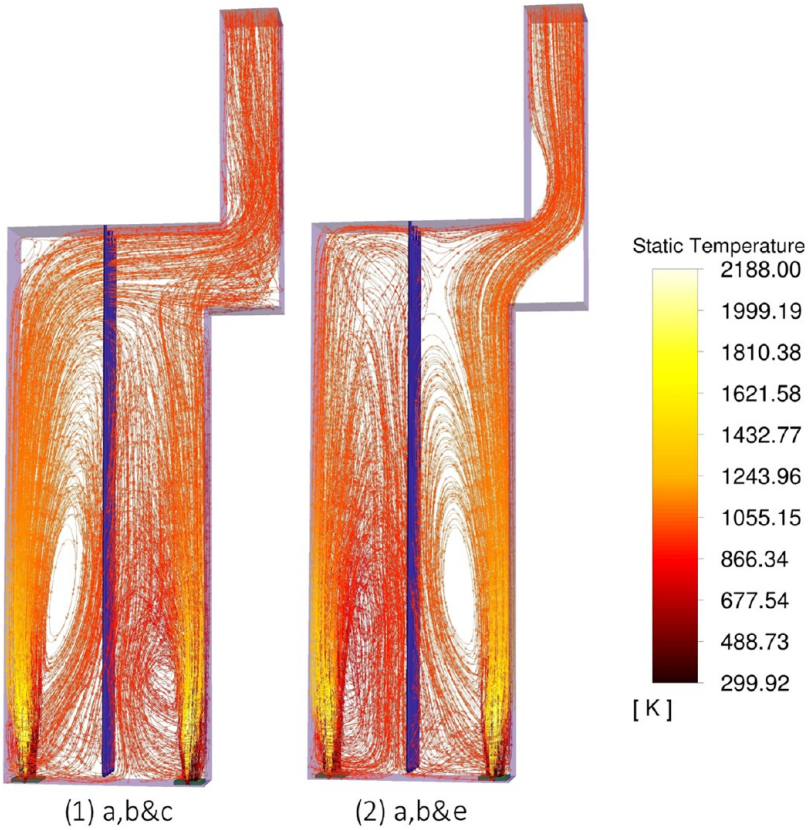

Figure 15. Streamlines of the flue gas colored by temperature within the furnace show two different states of clogging: (1) burners a, b, and c simultaneously; (2) burners a, b, and e simultaneously.

burners, temperatures increase after 2 min due to the decrease in process fluid temperature inside the coil, which reduces the driving force for heat transfer. Consequently, blocked burners disrupt the cracking process in these cells.

https://doi.org/10.1021/acsomega.4c00395
ACS Omega 2024, 9, 14500−14519

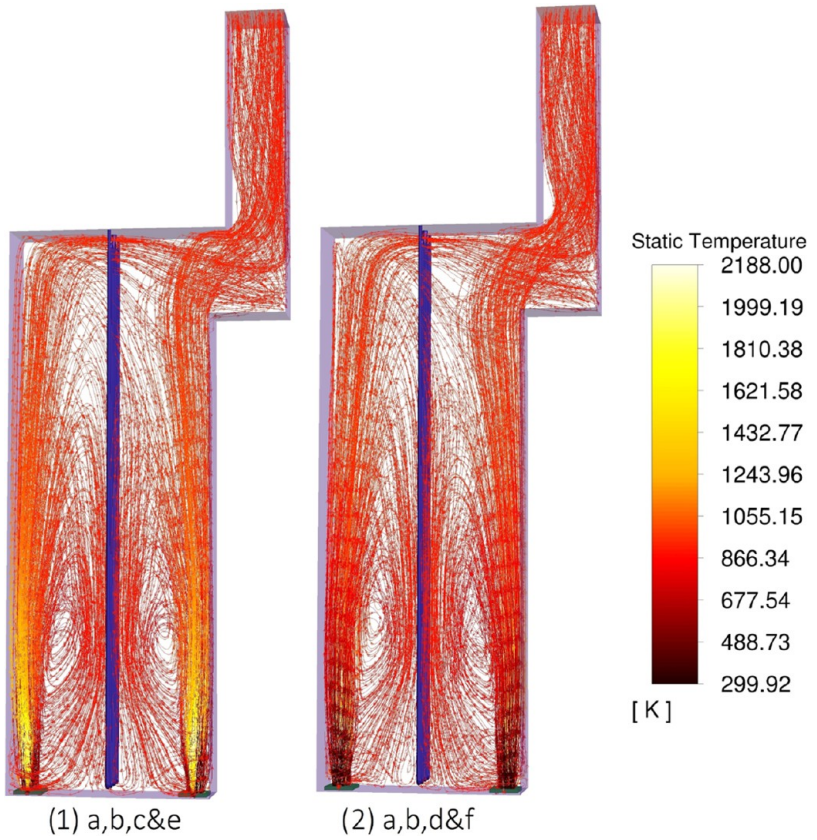

Figure 16. Streamlines of the flue gas colored by temperature in the furnace for two different states of clogging: (1) burners a, b, c, and e clogged; (2) burners a, b, d, and f clogged.

The streamlines created from different clogging scenarios are shown in Figures 13, 14, and 15, and the names of different cases of blockage are given at the top of Figure 13.

Figures 14, 15, and 16 illustrate the effects of burner clogging, revealing not only a reduction in temperature but also changes in the symmetry and uniformity of flow behavior in the furnace. Specifically, when burner a is blocked (Figure 14), the vortexes formed by combustion products exhibit nonuniform behavior, with an additional vortex formed in the upper part before the combustion chamber's exit area. Furthermore, the path through which the combustion products of the right burners exit is altered. Furthermore, a temperature drop on the right side of the furnace was observed, while the burners on the left side, which were all in service, had a higher temperature. A similar behavior happened for clogged burner b, which is symmetric with burner a. If both burners a and b were clogged, hydrodynamic symmetric conditions were created throughout the furnace, while the temperature dropped dramatically. The hydrodynamic behavior of the blocked burners a and b resembles the normal state. However, when type 2 burners (Figures 15 and 16) are clogged, noticeable changes occur in their hydrodynamic behavior. As depicted in Figures 15 and 16(1),16(2), turbulence stems from increased irregularities and the lack of symmetrical behavior in gas fuel input compared to that in the normal state. Ultimately, as the number of blocked burners increases, the temperature inside the furnace decreases.

Table 4 indicates the effects of coil outlet temperature and flue gas at the arch zone temperature for different states of burner clogging. According to the simulation results, the effect of clogging on COT as a key parameter in cracking furnaces is very noticeable. In the cracking mode, the effect of burner clogging on COT can decrease the yield of ethylene and propylene, which can result in undesirable products. As the temperature deviates from the standard and normal range of COT, the composition of the cracking products changes completely, and the cracking process is practically disrupted. In addition, burner clogging in steam-cracking furnaces can notably impact the arch temperature. The flue gas temperature generated in the radiation zones plays a critical role in producing very high-pressure (VHP) steam in the convection zone, which serves as the driving force for the turbine compressor of the cracked gas.

Table 4. CFD Simulation Results of Coil Outlet Temperature and Flue Gas at Arch Zone Temperature for Different States of Burner Clogging

clogged burners	COT (K)	Arch-T
normal	1070.18	1095
burner a	1024.99	1048.29
burner b	1030.7	1083.89
burners a and b	987.6	1005.6
burners a, b, and c	940.05	958.8
burners a, b, and e	941	978
burners a, b, c, and e	893.2	912
burners a, b, d, and f	893.62	913.8

According to the findings presented in Table 4 and considering the relatively symmetrical geometric conditions for burners a and b, the effect of burner clogging on the Arch temperature and process fluid temperature in steam-cracking furnaces varies depending on the specific burner. When burner

https://doi.org/10.1021/acsomega.4c00395
ACS Omega 2024, 9, 14500−14519

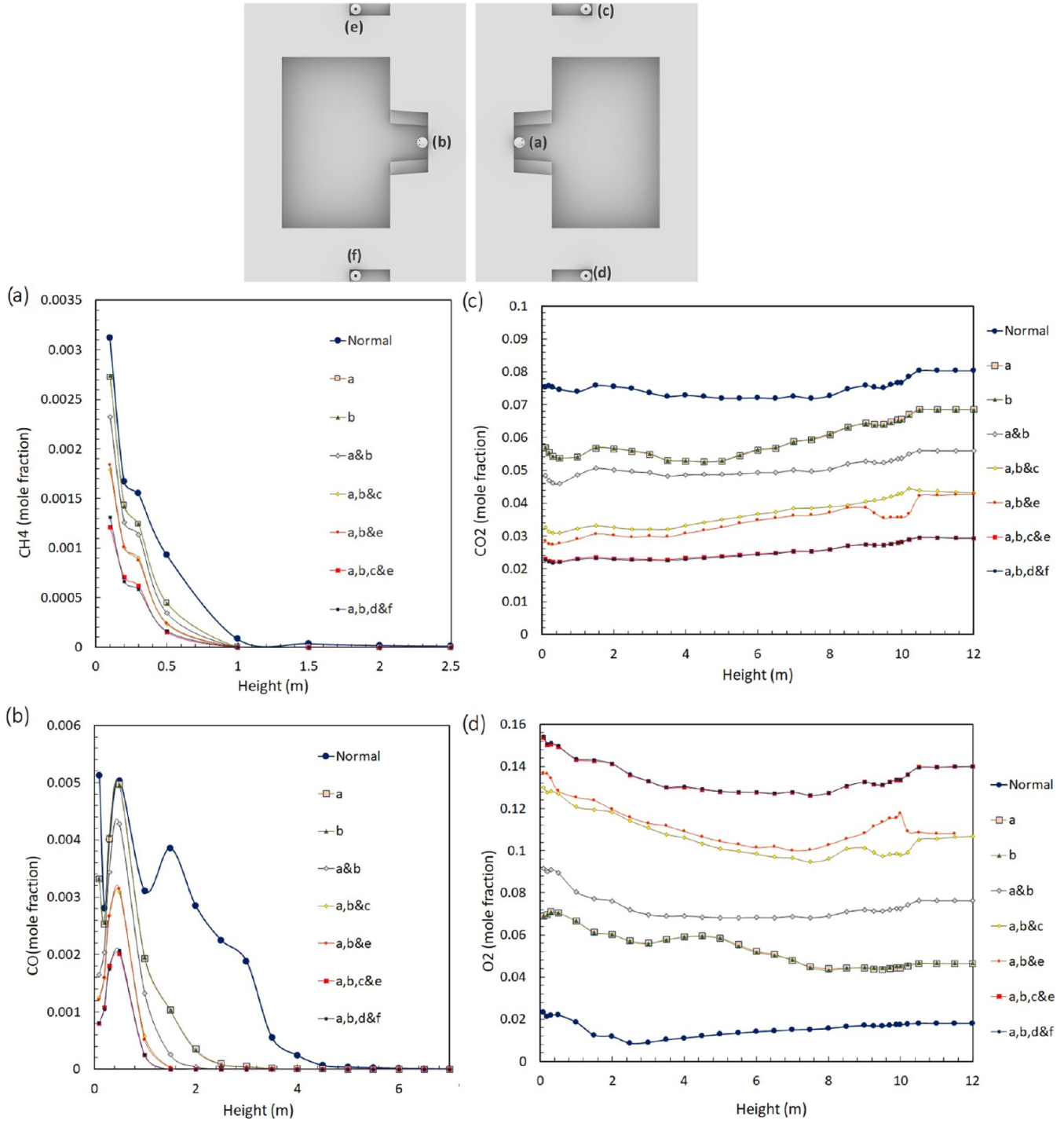

Figure 17. Average species profiles of (a) CH_4, (b) CO, (c) CO_2, and (d) O_2 along the furnace height for the different burner clogging scenarios depicted in the top graph.

a is blocked, both the temperature of the combustion products in the arch zone and the temperature of the process fluid at the outlet of the coil experience a more significant decrease compared to that when burner b is clogged. Severe clogging can severely disrupt the heat transfer between the coil and combustion chamber, leading to insufficient heat exchange. As a result, the desired cracking reactions may not occur optimally, potentially producing undesired byproducts.

To investigate the effect of different states of burner clogging on the composition of combustion products along the height of the furnace, the changes in the CH4, CO, CO_2, and O_2 mole fraction during the height of the furnace have been evaluated and are displayed in Figure 17.

According to Figure 17a, the amount of entered fuel gas has gradually decreased, and in almost all states of burner clogging, the fuel gas has completely reacted and converted into combustion products before reaching the height of one m of the furnace. At the same time, the patterns of methane consumption were similar for all situations, and the higher the amount of clogging, the less amount of inlet methane. Considering the fact that the excess air was 10% in the normal state as well, the fuel gas was consumed entirely, and

https://doi.org/10.1021/acsomega.4c00395
ACS Omega 2024, 9, 14500−14519

combustion products were produced before the height of two meters. Figure 17b illustrates the average distribution of the production of CO species for different clogging conditions along the furnace. With the reduction of fuel gas input due to the clogging of different burners, CO production also decreased since the amount of fuel gas input decreased, and less product was produced. The amount of CO for each state has increased up to a certain height and then converted to CO_2. In a normal state with the maximum amount of fuel gas input, all of the amount of CO has been consumed up to a height of 5 m. It is also evident that for cases where the burners are symmetrical, like burners a and b, the same results have been observed. Although different temperatures were obtained at the exit, they had symmetrical conditions at the entrance. CO_2 is continuously produced as a significant combustion product, and the average distribution result is shown in Figure 16c. The production of CO_2 has been reduced with the reduction of the fuel gas input, which is the result of clogging of the burners. According to Figure 16d, which indicates the average distribution of the O_2 species, the amount of fuel gas input has been reduced in the case of clogged burners, while the amount of input air was constant. As the burners became more clogged, more additional air entered the furnace, and finally, the amount of oxygen increased.

4.3. Influence of Holes on the Body of Burners. The small holes incorporated on the body of industrial non-premixed burner tips in the radiation zone of steam-cracking furnaces play a vital role in promoting efficient combustion. These holes serve to enhance the mixing between the fuel gas and the inlet air, thereby improving the combustion performance. When these holes are unobstructed, they facilitate the entry of fuel gas at multiple points, allowing for better distribution and dispersion throughout the combustion zone. This promotes more uniform mixing of fuel gas with the incoming air, leading to improved combustion efficiency, reduced emissions, and enhanced thermal efficiency. Due to the small size of these holes, there was a possibility that they would be blocked during the operation, although the burner was not blocked. Therefore, it seems that the effect of investigating their importance on the furnace's performance is important. In this section, the importance of the small holes applied to the body of the burners has been investigated and simulations have been performed in the absence of these holes. This analysis provides valuable insights into the importance of these small holes and makes clear their role in ensuring optimal burner performance in steam-cracking furnaces.

According to Figure 18, the results of the temperature distribution of combustion gases along the height of the furnace were compared to the normal state where these holes exist. Based on the results of the CFD simulation, a significant difference was observed in the results of these two states. Figure 18 demonstrates that the combustion operation was delayed at the bottom of the furnace for the case where the hole was absent (or had been clogged) and the temperature was significantly reduced. The decrement in temperature continued up to a height of 6 m, and after that, the temperature increased in comparison with normal state, and finally left the combustion chamber with a higher temperature.

Figure 19 showcases the streamlines of fuel gas and inlet air for two distinct states: the normal state of the burner and the burner without holes. This graphical representation highlights the significance of these holes. In the normal state, where the holes are present, efficient mixing is observed in the fuel and air

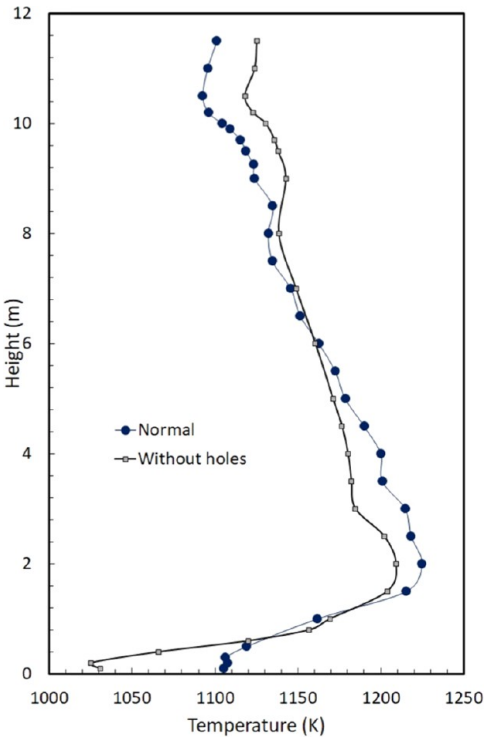

Figure 18. Results of the average temperature distribution of flue gas along the furnace height for two different states of the normal operation and without holes on the body of burners.

region. Conversely, the lack of these perforations hinders the mixing process in the burner without holes. The figure serves as compelling visual evidence that incorporating holes in the burner body facilitates effective mixing between the fuel gas and the inlet air, thereby emphasizing their crucial role in optimizing the combustion performance. Figure 19a,c provides compelling evidence of the impact of hole existence, wherein air injection and subsequent mixing occur at the initial stages of air entry, thereby triggering the combustion process. In Figure 19d, the fuel gas flow exiting the burner is observed to ascend to higher elevations within the furnace without interacting with the surrounding air. However, upon air entry, combustion transpires at these elevated positions. This phenomenon is apparent in Figure 19b, where the cold inlet flow enters the furnace. The absence of initial air-fuel gas mixing results in reduced turbulence, causing the air and fuel gas flows to follow regular trajectories upon entering the furnace.

Considering the design characteristics of type 1 burners, two angled holes induce a directional tilt in the airflow toward the wall, reducing the distance it traverses without reaction and accelerating the combustion process. The significance of these holes cannot be understated, warranting further investigations of their geometric optimization. Moreover, exploring methods to minimize clogging in operating furnaces is imperative, emphasizing the need for additional studies on geometric design considerations and optimal performance.

Figure 20 shows contour plots of the temperature distribution in the combustion zone of the furnace for the case without holes in the body. In this case, the temperature contour range is considered the same as that of the normal state (Figure 10) to facilitate a comparison. However, the maximum temperature obtained in this situation is lower than

https://doi.org/10.1021/acsomega.4c00395
ACS Omega 2024, 9, 14500−14519

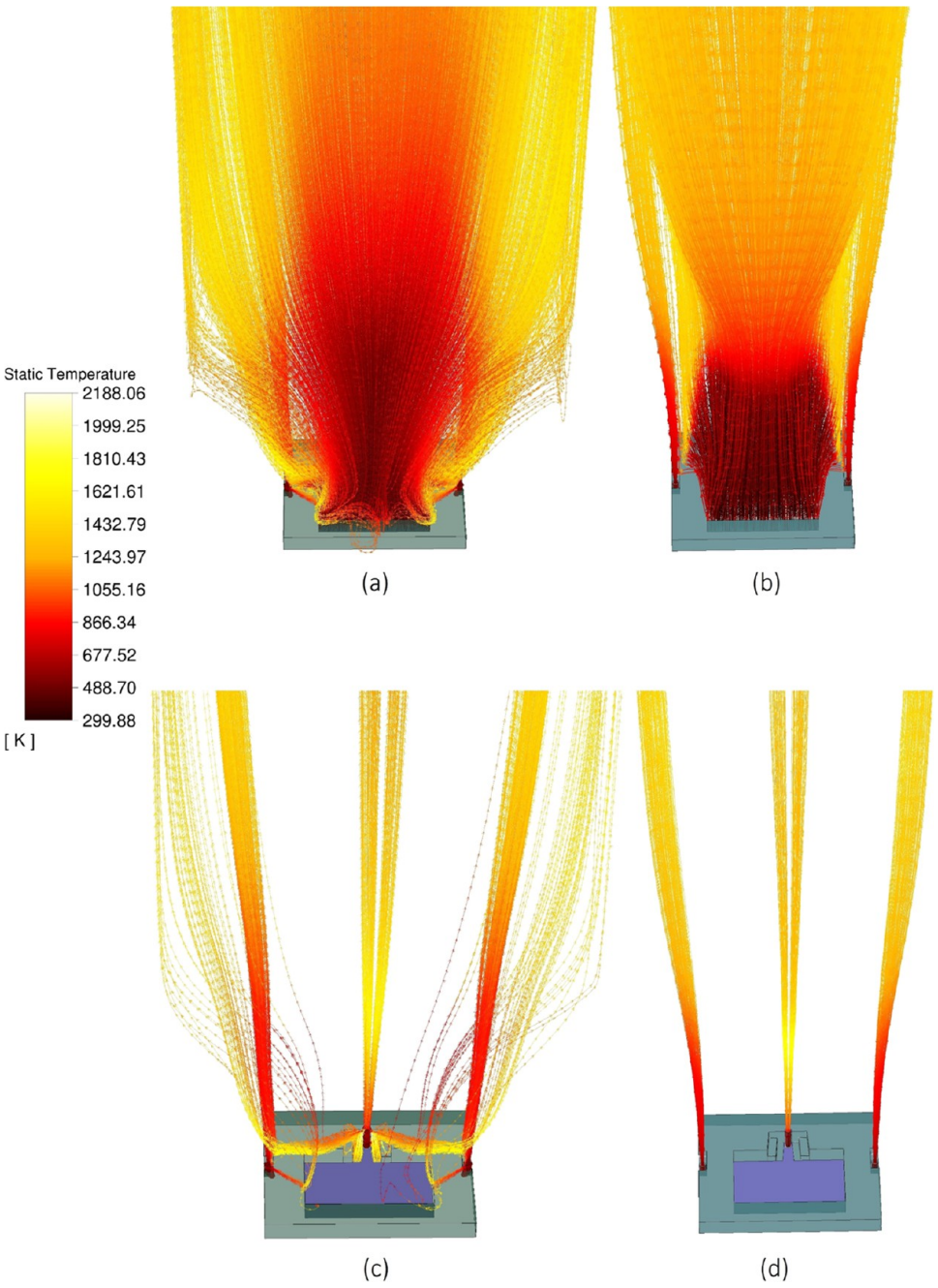

Figure 19. Comparison of streamlines of fuel gas and inlet air for two different states: (1) (a, c) normal condition and (2) (b, d) without holes on the body of burners.

that of the normal state. The outlet temperature is approximately 2021 K. Figure 20a,c indicates the range of air entry, where there was more cold air in the furnace due to a lack of proper initial mixing. Generally, the premixing of air and fuel gas in cracking furnaces increases the performance of the combustion process since a homogeneous flow is created, which provides a stable flame and uniform temperature distribution in the furnace. Thus, the installation of holes on burners plays the role of premixing and raises the efficiency of the combustion process in the furnace. Therefore, the proper design as well as the periodic maintenance and cleaning during the operation is of great importance.

The temperature profile of flow inside the coil is displayed in Figure 21. As can be obtained, in the initial areas of the coil, due to the greater driving force, the slope of temperature changes is steep as well, while moving toward the end of the coil area, the temperature rises with a slight slope.

5. CONCLUSIONS

In conclusion, this study successfully employed 3D CFD simulations to investigate the combustion performance of an industrial furnace in an olefin unit. The developed CFD model accurately predicted the heat release pattern and combustion behavior in the furnace, as validated by comparisons to industrial data. The average relative error for the CFD-predicted coil outlet temperature compared to industrial measurements was approximately 0.94% for the case of 10%

https://doi.org/10.1021/acsomega.4c00395
ACS Omega 2024, 9, 14500−14519

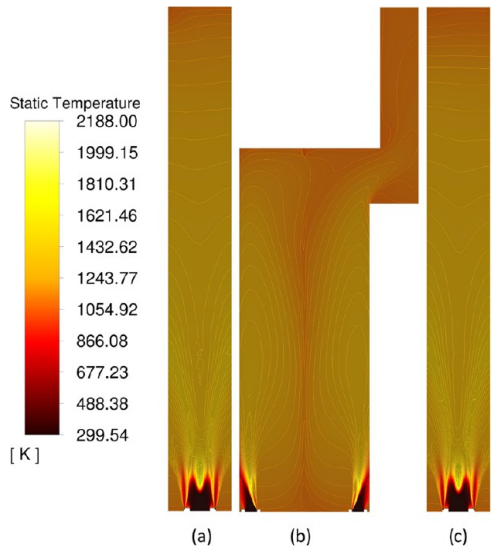

Figure 20. Contour plots of temperature distribution in the combustion zone of the furnace from three different views (without holes on the body of the burners).

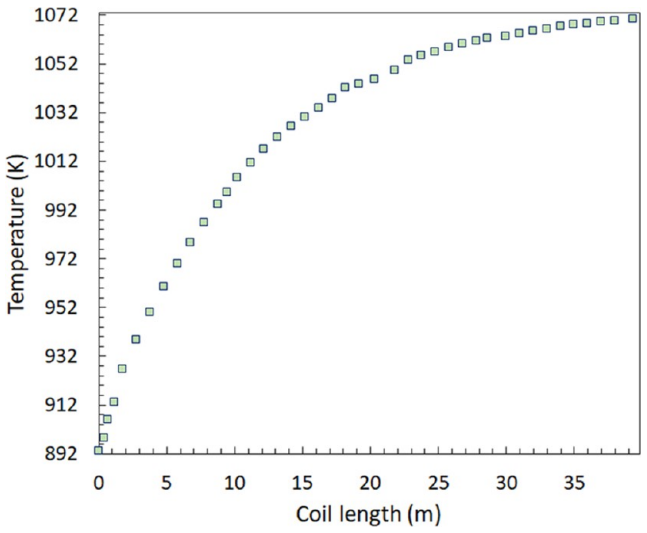

Figure 21. Temperature profile of process flow inside the coil.

excess air. Similarly, for the Arch temperature, the average relative error was around 1.108%.

The study extensively investigated burner clogging, conducting a thorough examination that involved blocking various types of burners to observe their effects. Critical parameters, such as the coil outlet temperature, flue gas temperature at the arch, combustion product composition, and flue gas flow dynamics, were carefully obtained. By systematically introducing clogging scenarios across different burner setups, the study unveiled significant impacts on furnace operation. These impacts included noticeable decreases in temperature, disruptions in symmetrical flow patterns, and changes in the fluid behavior. These findings underscore the detrimental effects of burner clogging on the furnace performance.

Furthermore, the study focused on the small holes present on the burner bodies and their crucial role in promoting efficient combustion, enhancing thermal efficiency and ensuring a stable and uniform temperature distribution. Simulations demonstrated that if these openings were assumed to be obstructed, as often observed in industrial burners of this type, then there were significant alterations in the thermal and hydrodynamic characteristics of the combustion gases. These results highlight the importance of refining burner designs and operational parameters to optimize production efficiency and reduce energy consumption and reduce emissions in steam-cracking furnaces.

AUTHOR INFORMATION

Corresponding Author

Seyyed Hossein Hosseini − *Department of Chemical Engineering, Ilam University, Ilam 69315-516, Iran;* orcid.org/0000-0003-3154-5903; Email: s.h.hosseini@ilam.ac.ir

Authors

Mohsen Fattahi − *Department of Chemical Engineering, University of Kurdistan, Sanandaj 66177-15175, Iran*

Saeed Ebrahimi − *Department of Chemical Engineering, Razi University, Kermanshah 67149-67346, Iran*

Masoud Rahimi − *Department of Chemical Engineering, Razi University, Kermanshah 67149-67346, Iran*

Maryam Gonbadi − *Department of Chemical Engineering, Faculty of Advanced Technologies, Shiraz University, Shiraz 71946-84471, Iran*

Goodarz Ahmadi − *Department of Mechanical and Aerospace Engineering, Clarkson University, Potsdam, New York 13699, United States*

Complete contact information is available at: https://pubs.acs.org/10.1021/acsomega.4c00395

Notes

The authors declare no competing financial interest.

ACKNOWLEDGMENTS

The authors acknowledge their respective departments for conducting the study.

NOMENCLATURE

x_i (m):spatial coordinate in the *i*-direction.
x_j (m):spatial coordinate in the *j*-direction.
ρ (kg/m^3):density of the fluid.
u_i (m/s):velocity components in the *i*-direction.
u_j (m/s):velocity components in the *j*-direction.
P_{eff} (Pa):effective pressure.
μ (Pa·s):dynamic viscosity.
μt (Pa·s):turbulent viscosity.
S_{ij} (1/s):rate-of-strain tensor components.
S_{Mi} (m/s^2):source term in the momentum equation due to gravitation in the *i*-direction.
H_{eff} (J/kg):effective enthalpy.
T (K):temperature.
λ (W/(m·K)):thermal conductivity.
λ_t (W/(m·K)):turbulent thermal conductivity.
α_k (m^2/s):turbulent diffusivity for turbulent kinetic energy.
α_ε (m^2/s):turbulent diffusivity for turbulent dissipation rate.
k (m^2/s^2):turbulent kinetic energy.
ε (m^2/s^3):turbulent dissipation rate.
P_k (m^2/s^3):turbulent production term for k.
$C_{1\varepsilon}$ (−):constant in the ε equation.
$C_{2\varepsilon}$ (−):constant in the ε equation.
C_μ (−):constant in the turbulent viscosity formulation.

https://doi.org/10.1021/acsomega.4c00395
ACS Omega 2024, 9, 14500−14519

Pr_t (−):turbulent Prandtl number.
η (−):- variable related to the turbulent quantities.
η_0 (−):reference value for η.
β (−):constant in the $C1\varepsilon$ equation.
ρH_{eff} (J/(m^3·s^2)):total enthalpy density.
S_{Mx} (m/s^2):source term in the momentum equation due to gravitation in the x-direction.
S_{My} (m/s^2):source term in the momentum equation due to gravitation in the y-direction.
S_{Mz} (m/s^2):source term in the momentum equation due to gravitation in the z-direction.
g (m/s^2):gravitational acceleration.
Q_{rad} (W/m^3):net volumetric heat release due to radiation.
P_1 (−):P_1 radiation model
q_r (J/s):net radiative heat transfer rate
G (−):incident radiation
a (−):absorption coefficient
σ_s (−):scattering coefficient
σ:(5.672 × W^{-8} W/m^2 K4):
n (−):refractive index of the medium
C (−):linear-anisotropic phase function coefficient
f (−):mixture fraction
$\bar{f}$ (−):mean mixture fraction
f^2 (−):variance of mixture fraction
m_f (−):mass fraction of fuel
m_0 (−):mass fraction of oxidizer
ρ (kg/m^3):density
$\bar{v}$ (m/s):mean velocity vector
φ (−):mean of a variable
$p_{(f)}$ (−):probability density function (PDF)
CFD:computational fluid dynamics
RNG:renormalization group
RANS:Reynolds averaged Navier−Stokes
DOM:discrete ordinates method
PDF:probability density function
COT:coil outlet temperature
VHP:very high pressure

REFERENCES

(1) Amghizar, I.; Vandewalle, L. A.; Van Geem, K. M.; Marin, G. B. New trends in olefin production. *Engineering* **2017**, *3* (2), 171−178.
(2) Rossi, F.; Rovaglio, M.; Manenti, F. Model Predictive Control and Dynamic Real-time Optimization of Steam Cracking Units. In *Computer Aided Chemical Engineering*; Elsevier, 2019; Vol. *45*, pp 873−897.
(3) van Goethem, M.; Oud, P.; Wijnja, J.-G.; Ramesh, R. Coil Design for Optimal Ethylene Yields. In *Computer Aided Chemical Engineering*; Elsevier, 2019; Vol. *45*, pp 831−872.
(4) Baukal, C. E. Industrial burners. 2003.
(5) Heynderickx, G. J.; Oprins, A. J.; Marin, G. B.; Dick, E. Three-dimensional flow patterns in cracking furnaces with long-flame burners. *AIChE J.* **2001**, *47* (2), 388−400.
(6) Oprins, A. J. M.; Heynderickx, G. J.; Marin, G. B. Three-dimensional asymmetric flow and temperature fields in cracking furnaces. *Ind. Eng. Chem. Res.* **2001**, *40* (23), 5087−5094.
(7) Lan, X.; Gao, J.; Xu, C.; Zhang, H. Numerical simulation of transfer and reaction processes in ethylene furnaces. *Chem. Eng. Res. Des.* **2007**, *85* (12), 1565−1579.
(8) Tutar, M.; Üstün, C. E.; Campillo-Robles, J. M.; Fuente, R.; Cibrián, S.; Arzua, I.; Fernández, A.; López, G. A. Optimized CFD modelling and validation of radiation section of an industrial top-fired steam methane reforming furnace. *Comput. Chem. Eng.* **2021**, *155*, No. 107504.
(9) Stefanidis, G.; Van Geem, K.; Heynderickx, G.; Marin, G. Evaluation of high-emissivity coatings in steam cracking furnaces using a non-grey gas radiation model. *Chem. Eng. J.* **2008**, *137* (2), 411−421.
(10) Gamil, A. A.; Nikolaidis, T.; Lelaj, I.; Laskaridis, P. Assessment of numerical radiation models on the heat transfer of an aero-engine combustion chamber. *Case Stud. Therm. Eng.* **2020**, *22*, No. 100772.
(11) Goebel, F.; Mundt, C. In *Implementation of the P1 Radiation Model in the CFD Solver NSMB and Investigation of Radiative Heat Transfer in the SSME Main Combustion Chamber*, 17th AIAA international space planes and hypersonic systems and technologies conference; AIAA, 2011; p 2257.
(12) Habibi, A.; Merci, B.; Heynderickx, G. J. Impact of radiation models in CFD simulations of steam cracking furnaces. *Comput. Chem. Eng.* **2007**, *31* (11), 1389−1406.
(13) Hu, G.; Schietekat, C. M.; Zhang, Y.; Qian, F.; Heynderickx, G.; Van Geem, K. M.; Marin, G. B. Impact of radiation models in coupled simulations of steam cracking furnaces and reactors. *Ind. Eng. Chem. Res.* **2015**, *54* (9), 2453−2465.
(14) Hosseini, A.; Hage, J. L. T.; Meijer, K.; Offerman, E.; Yang, Y. On the Importance of Model Selection for CFD Analysis of High Temperature Gas-Solid Reactive Flow; Case Study: Post Combustion Chamber of HIsarna Off-Gas System. *Processes* **2023**, *11* (3), No. 839, DOI: 10.3390/pr11030839.
(15) Wéry, F.; Geerts, M.; Vandewalle, L. A.; Reyniers, P. A.; Heynderickx, G. J.; Marin, G. B.; Van Geem, K. M. Assessing the CO2 emission reduction potential of steam cracking furnace innovations via computational fluid dynamics: From highemissivity coatings, over coil modifications to firing control. *Chem. Eng. Res. Des.* **2023**, *190*, 129−142.
(16) Wéry, F.; Geerts, M.; Vandewalle, L. A.; Reyniers, P. A.; Heynderickx, G. J.; Marin, G. B.; Van Geem, K. M. Optimizing air distribution in floor and wall burners of an industrial steam cracking firebox: a CFD study. *Chem. Eng. Res. Des.* **2023**, *199*, 569−582, DOI: 10.1016/j.cherd.2023.10.017.
(17) Yakhot, V.; Orszag, S.; Thangam, S.; Gatski, T.; Speziale, C. Development of turbulence models for shear flows by a double expansion technique. *Phys. Fluids A* **1992**, *4* (7), 1510−1520.
(18) Hu, G.; Wang, H.; Qian, F.; Van Geem, K. M.; Schietekat, C. M.; Marin, G. B. Coupled simulation of an industrial naphtha cracking furnace equipped with long-flame and radiation burners. *Comput. Chem. Eng.* **2012**, *38*, 24−34.
(19) Zhang, Y.; Qian, F.; Zhang, Y.; Schietekat, C. M.; Van Geem, K. M.; Guy, A.; Marin, G. B. Impact of flue gas radiative properties and burner geometry in furnace simulations. *AIChE J.* **2015**, *61* (3), 936−954.
(20) Bakker, A.; Haidari, A.; Marshall, E. M. Design reactors via CFD. *Chem. Eng. Prog.* **2001**, *97* (12), 30−39.
(21) Liu, B.; Bao, B.; Wang, Y.; Xu, H. Numerical simulation of flow, combustion and NO emission of a fuel-staged industrial gas burner. *J. Energy Inst.* **2017**, *90* (3), 441−451.
(22) Rohani, B.; Wahid, M.; Sies, M. M.; Saqr, K. M. In *Comparison of Eddy Dissipation Model and Presumed Probability Density Function Model for Temperature Prediction in a Non-Premixed Turbulent Methane Flame*, AIP Conference Proceedings; American Institute of Physics, 2012; pp 384−391.
(23) Ariwibowo, T. H.; Safitra, A. G.; Santoso, H. In *Investigation on Combustion Characteristics of Nonpremixed Combustion in an 85 MWe Wall Firing Boiler under Various Air-Fuel Ratio Using CFD*, 2017 International Electronics Symposium on Engineering Technology and Applications (IES-ETA); IEEE, 2017; pp 20−26.
(24) Mahmoodi, B.; Hosseini, S. H.; Ahmadi, G.; Raj, A. CFD simulation of reactor furnace of sulfur recovery units by considering kinetics of acid gas (H2S and CO2) destruction. *Appl. Therm. Eng.* **2017**, *123*, 699−710.
(25) Mahmoodi, B.; Hosseini, S. H.; Raj, A.; Hooman, K. A new acid gas destruction kinetic model for reaction furnace of an industrial sulfur recovery unit: A CFD study. *Chem. Eng. Sci.* **2022**, *256*, No. 117692.
(26) Setarehshenas, N.; Hosseini, S.; Esfahany, M. N.; Ahmadi, G. Impacts of solid-phase wall boundary condition on CFD simulation of

https://doi.org/10.1021/acsomega.4c00395
ACS Omega 2024, 9, 14500−14519

conical spouted beds containing heavy zirconia particles. *J. Taiwan Inst. Chem. Eng.* **2016**, *64*, 146−156.
(27) Xiong, M.; Chen, B.; Zhang, H.; Qian, Y. Study on Accuracy of CFD Simulations of Wind Environment around High-Rise Buildings: A Comparative Study of k-ε Turbulence Models Based on Polyhedral Meshes and Wind Tunnel Experiments. *Appl. Sci.* **2022**, *12* (14), No. 7105, DOI: 10.3390/app12147105.
(28) Sosnowski, M.; Gnatowska, R.; Sobczyk, J.; Wodziak, W. Numerical Modelling of Flow Field within a Packed Bed of Granular Material. *J. Phys.: Conf. Ser.* **2018**, No. 012036, DOI: 10.1088/1742-6596/1101/1/012036.
(29) Zhang, H.; Tang, S.; Yue, H.; Wu, K.; Zhu, Y.; Liu, C.; Liang, B.; Li, C. Comparison of computational fluid dynamic simulation of a stirred tank with polyhedral and tetrahedral meshes. *Iran. J. Chem. Chem. Eng.* **2020**, *39* (4), 311−319.
(30) Sosnowski, M.; Krzywanski, J.; Gnatowska, R. In *Polyhedral Meshing as an Innovative Approach to Computational Domain Discretization of a Cyclone in a Fluidized Bed CLC Unit*, E3S Web of Conferences; EDP Sciences, 2017; p 01027.

https://doi.org/10.1021/acsomega.4c00395
ACS Omega 2024, 9, 14500−14519